A PARAMETRIC STUDY OF TRANSONIC BLADE-VORTEX INTERACTION NOISE

A. S. Lyrintzis, Assistant Professor
Y. Xue, Research Assistant

Aerospace Engineering and Mechanics
University of Minnesota
Minneapolis, MN 55455-0153

Principal Investigator: A. S. Lyrintzis

Final Report, Contract No. NAG 6-626 (7/1/90-6/30/91)

Abstract

Several parameters of transonic blade-vortex interactions (BVI) are being studied and some ideas for noise reduction are introduced and tested using numerical simulation. The model used is the two-dimensional high frequency transonic small disturbance equation with regions of distributed vorticity (VTRAN2 code). The far-field noise signals are obtained by using the Kirchhoff method which extends the numerical two-dimensional near-field aerodynamic results to the linear acoustic three-dimensional far-field. The BVI noise mechanisms are explained and the effects of vortex type and strength, and angle of attack are studied. Particularly, airfoil shape modifications which lead to noise reduction are investigated here. The results presented are expected to be helpful for better understanding of the nature of the BVI noise and better blade design.

Introduction

In recent years, helicopters have proved to be convenient and reliable means of transportation, because of their ability to take off, land and maneuver in areas inaccessible to fixed wing aircraft. Helicopter aerodynamics are very complex, because three-dimensional, unsteady, transonic, viscous, aerodynamic phenomena are involved. (An excellent survey of helicopter aerodynamics can be found in a recent review paper by Johnson [1].) The increasing use of helicopters in both military and civilian applications has drawn attention to the noise that they generate. In civilian applications this noise can be very annoying and in military applications provides early warning of a helicopter's approach. Internal noise problems make helicopters unattractive to prospective civilian passengers and in the military often substantially exceed acceptable limits. Noise in the design of new or modified helicopters is today a matter of great concern. The helicopter noise rules (Appendix H to Federation Aviation Regulations (FAR) Part 36) contain the helicopter noise levels for which compliance must be shown for actual flight tests. Depending on the maximum certified weight of the helicopter, the maximum allowable noise levels are between 88 and 108 EPNdB(Effective Perceived Noise Lever) for flyover, 90 and 110 EPNdB for approach, and 89 and 109 for the takeoff condition. It should be reiterated that these standards are applicable to all type certification applications received on or after March 6, 1986 [2]. In order to comply with these rules, the designer must have very good estimates of the detailed noise characteristics of the proposed rotorcraft.

Among the several types of helicopter noise [3], that due to Blade Vortex-Interactions (BVI) is one of the most important. When present, BVI leads to high levels of vibration and to intense noise radiation. A great deal of computational and experimental effort is being expended to minimize the adverse effects of BVI, so that structural fatigue and acoustic detectability can be reduced, and crew and passenger comfort and noise abatement can be improved. Advances in those areas will lead to significant increases in productivity, public acceptance, and the competitiveness of the U. S. rotorcraft industry.

BVI is the aerodynamic interaction of a rotor blade with the trailing vortex system generated by preceding blades as shown in figure 1 (from reference [4]). In level steady-state flight the induced velocity of the rotor disk tends to make all the tip vortices pass under the rotor disk. However, during steady descending flight or maneuvers the tip vortices are forced into the rotor disk plane causing strong blade-vortex interactions. The occurrence of BVI is very sensitive to rotor design parameters and helicopter operating conditions and has a profound impact on helicopter performance. When it occurs BVI is loud, impulsive in character, and tends to dominate the other noise sources, as shown experimentally (e.g. Schmitz and Yu [5]).

The newly developed tilt rotor aircraft also have some complicated three-dimensional BVI geometries that generate far-field noise [6]. The design characteristics of the tilt rotor aircraft make it a suitable candidate for short-to-medium range commercial transport applications. One of the important issues though, is the effect of the generated noise on the community and the passengers. Tilt rotor aircraft have additional operational options. For example, descent can be accomplished with high or low nacelle tilt, high or low glide slope, different airspeeds, etc. Even for a given nacelle tilt and flight path, lift can be distributed differently between rotors and wing. Thus, an optimization study of tilt rotor operations for noise reduction should be carried out. Also, tilt rotor aircraft have more complicated acoustic mechanisms than helicopters for various reasons. Previous experimental studies show that one of the dominating mechanisms during descent is blade-vortex interaction.

The noise reduction and prediction capabilities are often achievable through experimental programs directed at understanding the noise source mechanisms and the effects of design and flight parameters on noise. Flight test or wind tunnel test programs can be used, but in either case

there are certain problems such as high expense, safety risks, atmospheric variability as well as reflection problems for wind tunnel tests. Therefore, numerical simulations with a proper model are being employed for the prediction of BVI noise because they are cheap and efficient, although a very accurate model for BVI noise has not yet been found for practical applications.

Interactions generate the most significant noise when they are intrinsically unsteady, as when the vortex is exactly or nearly parallel to the blade. Incompressible BVI have been successfully treated in the past [7]. For typical helicopter cases it was shown in references [8] and [9] that the aerodynamics and aeroacoustics of the interactions are transonic. In such cases the flow can be initially modeled by two-dimensional unsteady transonic flow (figure 2).

Unsteady transonic flow problems have been solved numerically in the past. The low frequency approximation of the unsteady two-dimensional Transonic Small Disturbance (TSD) equation was first solved by Ballhaus and Goorjian [10] and the LTRAN2 code was created. Since then the code has been updated to include high frequency effects [11], viscosity [12], monotone switches [13] and second order effects [14]. However, the acoustic waves resulting from the unsteady motion have not been adequately studied.

Two-dimensional transonic BVI was first studied computationally in the near- and mid-field by George and Chang [8, 9] who used the high frequency transonic small disturbance equation, including regions of convected vorticity. References [8, 9] also contain detailed discussions of the background and formulation of the transonic BVI problem. A comprehensive code, VTRAN2 was developed [15, 16]. The vorticity is bilinearly distributed inside a vortex core and branch cuts are introduced in the x-direction. The vortex can either follow a prescribed path, or be convected with the free stream. A new look at the physics of the acoustics of unsteady transonic flow, especially around an oscillating flap, was given in reference [17].

In references [18-24] the two-dimensional transonic BVI problem is also solved using the small disturbance theory and the more complex Euler and thin-layer Navier Stokes equations. Also Baeder *et al.* [24, 25] presented some near- and mid-field results. A direct comparison of the results obtained from the different methods (from small disturbance to Navier Stokes equations) shows that the results are very similar [9]. In fact the results tend to coincide the further away we move from the airfoil surface. At great distances from the airfoil though, the waves become very difficult to follow because of numerical diffusion and dispersion errors, which led us to use the Kirchhoff method.

The Kirchhoff method was introduced [16, 27-32] to extend the numerically calculated nonlinear aerodynamic near-field results to the linear acoustic far-field. This method uses a Green's function for the linearized governing equation to derive a representation for the solution in terms of its values and derivatives on a closed surface S in space, which is assumed to include all the nonlinear flow effects and noise sources. The potential and its derivatives can be numerically calculated from a nonlinear aerodynamic code (e.g. VTRAN2). The Kirchhoff method has the advantage of including the full diffraction effects and eliminates the erroneous propagation of the reactive near-field.

In this report we first present some discussion of the BVI noise source mechanisms, which leads to ideas for noise reduction on transonic BVI noise. Typical results for types A, B and C shock motions are shown. Some typical results are shown in comparison to other methods. Directivity is shown for different coordinate systems. Then ideas and numerical tests for noise reduction are introduced. The results are shown for the airfoil (NACA64A006) shape modification achieved through the addition to various portions of the airfoil lower surface of cosine or NACA 4-digit shapes of different maximum thickness. These results give us ideas of how to modify the shape of the airfoil for noise reduction. An example of a modified airfoil (SC1095rn) is also demonstrated. Then, we show results for the splitting vortex model, variations of vortex strength and increasing angle of attack, parameters that could be adjusted for noise reduction. Finally,

some results for future experimental BVI cases are shown. Some of those results were also reported in reference [32], but a more detailed discussion is given here.

The Numerical Method (VTRAN2)

VTRAN2 is a code [15, 16] developed for analyzing the interactions of convected regions of vorticity with airfoils using transonic small disturbance theory. It is based on the ADI implicit scheme of the LTRAN2 code [10] with the inclusion of the high frequency term as described in reference [11] and the addition of regions of convected vorticity using the cloud-in-cell and multiple branch-cut approach. The code was modified to include viscosity [12] and monotone switches [13].

The equation for the unsteady transonic small-disturbance potential ϕ is:

$$A\phi_{tt} + 2B\phi_{xt} = C\phi_{xx} + \phi_{yy} \tag{1}$$

where

$$A = \frac{k^2M^2}{\delta^{2/3}}, \quad B = \frac{kM^2}{\delta^{2/3}}, \quad C = \frac{1-M^2}{\delta^{2/3}} - (\gamma+1)M^m \phi_x ,$$

ϕ is the disturbance-velocity potential, M is the free-stream Mach number, δ is the airfoil thickness ratio and k is the reduced frequency $\omega c/U_o$ where ω is the characteristic frequency of the unsteady motion, c is the airfoil chordlength and U_o is the free stream velocity. The quantities x, y, t, ϕ in equation 1 have been scaled by c, $c/\delta^{1/3}$, ω^{-1}, and $c\delta^{2/3} U_o$, respectively. The exponent m in the nonlinear term is chosen as m = 2, which is suitable for stronger shocks as it locates the shocks more accurately [33].

For BVI the characteristic frequency of the motion depends on the lateral distance between the airfoil and the vortex path. For large miss distances y_v the characteristic frequency ω is U_o/y_v and thus $k=c/y_v<<1$. Therefore, the k^2 term in A implies that the first term (i. e. high frequency term) in equation (1) can be dropped giving the low frequency small disturbance theory, which was used in the LTRAN2 code. However, for BVI cases of interest $y_v \approx c$, and thus $k \approx 1$ and the full small disturbance equation (1) (including the high frequency term) is needed. Since time t is nondimensionalized, the choice of k for the case of BVI is irrelevant and was taken as k=1 ($\omega=U_o/c$), meaning that one time unit corresponds to a free stream convection of one chord.

The boundary conditions are:

1. Upstream outer boundary condition:

$$\phi_x = \phi_y = 0 \qquad \text{as } x \to -\infty \tag{2}$$

2. Lateral outer boundary condition:

$$\phi_x = \phi_y = 0 \qquad \text{as } y \to \pm\infty \tag{3}$$

3. Downstream outer boundary condition:

$$\phi_x + k\,\phi_t = 0 \qquad \text{as } x \to +\infty \tag{4}$$

4. Airfoil surface boundary condition (applied at y=0):

$$\phi_y = \frac{\partial Y\pm}{\partial x} + k\,\frac{\partial Y\pm}{\partial t} \qquad \text{as } 0 < x < c \tag{5}$$

where $Y\pm$ defines the airfoil surface. The boundary conditions are summarized in figure 3.

For the viscosity calculations the viscous ramp method (wedge) is used. The viscous ramp model simulates the shock/boundary layer interaction by placing a wedge-nosed ramp at the base of the shock to obtain the reduced shock pressure rise. The surface geometry must be augmented by the ramp model by adding an extra viscous term in the boundary condition of equation (5). Details of the calculation of that viscous term can be found in reference [34]. The ramp model was derived for steady-state computations. However, it can be incorporated into unsteady computations in a quasi-steady fashion. Thus, the model is valid for low frequencies, and its use in high frequency problems such as BVI can only give some qualitative information about the effect of viscosity with almost no additional CPU time. The more complicated and CPU time-consuming lag-entrainment method which was also incorporated in our code was not used, because it was not superior to the wedge model for unsteady cases [34].

The classical Kutta condition is satisfied by this small disturbance formulation. We are interested in cases for which the reduced frequency range is less than 4, which is the limit for the application of the Kutta condition [35].

The pressure coefficient C_p in the unsteady small-disturbance theory is:

$$C_p = -2\delta^{2/3}(\phi_x + k\,\phi_t) \tag{6}$$

In addition, the wake condition

$$\Gamma_x + k\Gamma_t = 0 \tag{7}$$

implies that a branch cut exists between the trailing edge and the downstream outer boundary, across which the potential jump is, $\Delta\phi = \Gamma$, where Γ is the circulation.

A finite vortex core is used (cloud-in-cell method) for reasons of computational stability. The core has a finite square shape limited by gridlines and the vorticity is bilinearly distributed inside. Thus, several branch cuts (in the x-direction) are introduced. The vortex can have a free path (convected by the flow) or a prescribed path (miss distance y_v = constant, vortex velocity=U_o). Details of the theoretical formulation were given by Chang [36] and Lyrintzis [16].

An alternating direction implicit (ADI) method is used for the solution of the equation, where the high frequency term is added in the y-sweep. An approximate factorization technique with monotone switches [13] is used for the steady calculation, which provides a start-up solution. Special care is taken for the conservative differentiation along the uneven mesh.

A (213x199) mesh is used for the calculations. The computational mesh points are clustered more densely near and in front of the airfoil and then are stretched exponentially from the near airfoil region to about 200 chords from the airfoil in x and 400 in y-direction. More mesh points are added in the y-direction for the more accurate evaluation of the normal derivatives on the Kirchhoff surface. It was shown in the past that the (213x199) mesh leads to smoother results than

the (213x119) mesh. The code has a high vectorization level and the CPU time for each two-dimensional case on a Cray-2 computer is about 4 minutes for 800 time-marching steps.

The numerical simulation method (VTRAN2 code) introduced above is simple and efficient. Also, it is able to catch the main features of transonic BVI, which are the shock motions around airfoils. The code was shown to agree well with other, more complex approaches including Euler and thin-layer Navier-Stokes computations [9]. Thus, we expect that our conclusions will also hold if more accurate Euler/Navier-Stokes predictions are used. Three-dimensionality will, of course, influence the results. Some of the presented results will hold for three-dimensional cases, but only actual three-dimensional calculations (e. g. [37]) can show that. However, at great distances from the airfoil the waves become very difficult to follow because of numerical diffusion and dispersion errors. Thus, in order to study the far-field a more accurate method is needed which must also include three-dimensional effects. First, we will examine the different methods used in acoustic studies.

Methods of Acoustic Analysis

Sound can be considered as the propagating part of the full solution of some fluid-flow problems. In a few cases the radiated sound can be found this way. However, in most cases of practical interest one cannot find a full numerical solution everywhere in the flow, because of diffusion and dispersion errors caused by increasing mesh size in the far-field. Thus, it is often advantageous, or even necessary, to develop ways of determining the far-field noise from near-field solutions. The various approaches used to find the far-field noise, as explained by George [38], can be classified as follows:

1) *Full Flow Field Solution*: This is a calculation of the full nonlinear flow field including far-field waves. An example of an application of this technique for the calculation of radiating waves in the mid-field from transonic blade-vortex interactions is given by Baeder *et al.* [25, 26]. However, in order to numerically resolve the details of the acoustic three-dimensional far-field very fine mesh should be used which makes these computations impractical for technically significant problems even with today's powerful supercomputers.

2) *Acoustic Analogy*: This is a nonlinear near-field solution plus the Ffowcs Williams and Hawkings equation. This approach starts from the calculation of the nonlinear near- and mid-field and the far-field is found from a linear Green's function formulation evaluated in terms of surface and volume integrals over the retarded time transformations of the near- and mid-field flow and body surfaces. We would note that there are substantial difficulties in including the nonlinear quadrupole term (which requires second derivatives) in the volume integrals, especially around shock surfaces. Thus, many investigators use near-field data only on the blade surface, which is less accurate since the effect of shocks is not accounted for. For a review of the applications of acoustic analogy the reader is referred to Farassat and Brentner [39].

3) *Nonlinear Near-field Plus Kirchhoff Method*: This is a calculation of the nonlinear near- and mid-field with the far-field solutions found from a linear Kirchhoff formulation evaluated on a surface surrounding the nonlinear-field. The full nonlinear equations are solved in the first region (near-field), usually numerically, and a surface integral of the solution over the control surface gives enough information for the analytical calculation in the second region (far-field). This method provides an adequate matching between the aerodynamic nonlinear near-field and the acoustic linear far-field. An advantage of the method is that the surface integrals and the first derivatives needed can be easily evaluated from the near-field CFD data; full diffraction and focusing effects are included while eliminating the propagation of the reactive near-field. The method is simple and accurate as it accounts for the shock-related noise in the far-field. This technique is the basis of this research.

Kirchhoff's Method

Kirchhoff's method is an innovative approach to the rotorcraft noise problem which takes advantage of the mathematical similarities between the aeroacoustic equations and the equations of classical electrodynamics. We propose to apply the considerable body of theoretical knowledge regarding electrodynamic field solutions to arrive at a creative and novel solution to a difficult problem of technological importance.

Kirchhoff's formula was first published in 1882. Morgans [40] derived a Kirchhoff formula for a moving surface using a lengthy and complicated analysis. Hawkings [41] and Morino [42-44] rederived that formula for some special cases using the Green's function approach. Recently, Farassat and Myers [45] rederived the general Kirchhoff formula for a moving deformable piecewise smooth surface using generalized derivatives.

Kirchhoff's formula has also been used in the theory of light diffraction and other electromagnetic problems (Jones [46], Stratton [47]), as well as in problems of wave propagation in acoustics (Pierce [48]). Hawkings [41] used this formula to predict the noise from high speed propellers and helicopter rotors. Korkan *et al.* [49, 50] calculated high speed propeller noise using the Kirchhoff formulation of Hawkings [51]. Morino [52, 53] used a Kirchhoff formulation for the development of boundary element methods. Purcel *et al.* [51, 52] and Baeder [53] used a modified Kirchhoff method including also some nonlinear effects to calculate high speed compressibility noise. Some examples of Kirchhoff method implementations are also given in reference [28]. The Kirchhoff method was also used in BVI [16, 27, 29-32] to extend the numerically calculated nonlinear aerodynamic BVI results to the linear acoustic far-field.

The Green's function approach pioneered by Morino [42-44] was chosen for its simplicity and because the coordinate system used is suitable for BVI calculations. The method uses a Green's function for the linearized governing equation to derive a representation for the solution in terms of its values and normal and time derivatives on a closed surface S in space, which is assumed to include all the nonlinear flow effects and noise sources. A full three-dimensional, compressible formulation is used, because in this case the Green's function is simpler and because the method is easily extended to include spanwise variations to model three-dimensional BVI. A brief discussion of the Kirchhoff formulation is given in the following paragraphs; for more details the reader is referred to the above references.

A Green's function for the linearized governing equation is used to derive a representation for the solution in terms of its values and derivatives on a closed surface S in space, which is assumed to include all the nonlinear flow effects and noise sources. A full three-dimensional formulation is used, because the Green's function is simpler in this case, and because the method can be easily extended to include spanwise variations to model three-dimensional BVI.

The Green's function G for the linear unsteady potential flow is the solution of the equation:

$$\nabla^2 G - \frac{1}{c_o^2}\left(U_o \frac{\partial}{\partial x} + \frac{\partial}{\partial t}\right)^2 G = \delta(x-x_1, y-y_1, z-z_1, t-t_1) \qquad (8)$$

where c_o is the speed of sound, U_o is the free stream velocity, subscript 1 implies the acoustic source, and here δ is the well known Dirac delta function. We should note that equation (2) is the same as equation (1) without the nonlinear terms. The Green's function G must satisfy the causality condition for hyperbolic equations

$$G = \frac{\partial G}{\partial t_1} = 0 \quad \text{for } t < t_1$$

The solution of equation (2) for the subsonic case is given by

$$G = -\frac{\delta(t_1 - t + \tau)}{4\pi r \beta} \tag{9}$$

where

$$r_o = \{(x-x')^2 + \beta^2[(y-y')^2 + (z-z')^2]\}^{1/2}$$

$$\tau = \frac{[r_o - M(x-x')]}{c_o \beta^2}$$

$$\beta = (1-M^2)^{1/2}$$

This result is well known (see, for example, Morino [42]). If we assume that all the acoustic sources are enclosed by an imaginary closed rigid surface S, then we can prove (Green's theorem) that the pressure distribution outside this surface S is given by:

$$p(x_o, y_o, z_o) = -\frac{1}{4\pi} \int_S \left(\frac{1}{r_o} \frac{\partial p}{\partial n_o} + \frac{1}{c_o r_o \beta^2} \frac{\partial p}{\partial t} \left(\frac{\partial r_o}{\partial n_o} - M \frac{\partial x'_o}{\partial n_o} \right) + \frac{p}{r_o^2} \frac{\partial r_o}{\partial n_o} \right)_\tau dS'_o \tag{10}$$

where " ' " denotes a point on the Kirchhoff surface, M is the free stream Mach number, c_o is the speed of sound, subscript o denotes the transformed values using the well known Prandtl-Glauert transformation:

$$x_o = x, \quad y_o = \beta y, \quad z_o = \beta z$$

n is the outward vector normal to the surface S, and subscript τ implies the evaluation at the retarded time $t_1 = t - \tau$.

Thus, the values of the pressure and its normal derivatives on an arbitrary surface around the spanwise extent of an arbitrary flow are enough to give the far-field radiation at any arbitrary external point. In our work we use a rectangular box coinciding with mesh points in order to simplify the computation. The control volume is shown in figure 4. The pressure and its derivatives can be numerically calculated from an aerodynamic near-field code.

Since Kirchhoff's method assumes that linear equations hold outside this control surface S, it must be chosen large enough to include the region of nonlinear behavior. However, due to increasing mesh spacing the accuracy of the numerical solution is limited to the region immediately surrounding the moving blade. As a result S cannot be so large as to lose accuracy in the numerical solution for the mid-field. Therefore, a judicious choice of S is required for the effectiveness of the Kirchhoff method. A rectangular box-shaped surface (figure 4) is used for the calculations. The VTRAN2 code is used to calculate the solutions on the surface S. The x-limits for S were varied between 0.15 and 0.50 chords and values of 0.25 chords upstream and downstream of the leading and trailing edges are chosen. The y limits of S for our calculations are varied over a range from $y_S = 0.25$ to 4.00 chords distance from the airfoil. Higher Mach numbers yield higher optimum values for y_S because of the stronger nonlinearities in the larger lateral extent

of the flow region, as expected from the scaling laws of transonic flow. The similarity parameter K ($K=(1-M^2)/\delta^{2/3}$, where d is the airfoil maximum thickness) can be used for the scaling of transonic flow. Figure 5 shows the dependance of y_s on the value of K and was derived from numerical experiments with our code for a (213x199) mesh.

Strip theory approximation is used, that is, the two-dimensional VTRAN2 solution is applied on different segments of the blade in a stripwise manner. Blade segments ranging from two to sixteen in aspect ratio are used. Usually mesh limitations keep the Kirchhoff surface close enough to the blade where the two-dimensional strip theory solution is still valid. It can be shown that the wake does not need to be included in S, since the pressure is continuous across it. The distributed vortex, being a region where the homogeneous equation is invalid, should be included within the surface S. However, the effect of including or not including the vortex is comparatively small, particularly as it is nearly unaccelerated while it is outside S. We verified this by trying calculations with surfaces which included and excluded the vortex when it was near the airfoil. By making calculations with or without the inclusion of the tip surfaces we found [28] that they have only a small effect; thus they were neglected for most of the calculations.

Finally, some effects for non-parallel blade-vortex interactions were studied in the past utilizing the Kirchhoff method formulation and strip theory [29]. We can simulate a vortex of arbitrary shape or sweep interacting with a blade using VTRAN2 results for a parallel BVI, varying the delay time for the different chordwise strips. This technique is limited to small intersection angles λ, as the three-dimensional effects become large in higher angles. However, it is expected to provide adequate information in small intersection angles. The same technique of delaying times can be used for any arbitrarily shaped vortex (i.e. circular vortex).

Types of Unsteady Shock Motion

Tijdeman [54] showed experimentally, using an oscillating flap, that varying airfoil surface boundary conditions can give three different types of unsteady shock motion: (figure 6)

Type **A** shock motion, where the shock at the rear of the supersonic region merely moves back and forth with concurrent changes in strength.

Type **B** shock motion, where the shock moves similarly to type A, but disappears temporarily during the unsteady motion.

Type **C** shock motion, where the supersonic region disappears, but a shock wave leaves the airfoil and propagates forward to the far-field.

The above three types of unsteady shock motions heavily affect the characteristics (e. g. lift, drag) of all unsteady transonic flows. The type of shock motion that occurs in a given situation depends on the flow characteristics (e. g. free stream Mach number, airfoil shape, amplitude and frequency of the unsteady motion). These types of shock motion can even be observed in steady airfoils with severe flow separation downstream of the shock waves. Their existence in BVI has been verified by different experiments and calculations (e. g. Tangler's experiments [55]).

Results and Discussion

Some mid-field calculations for BVI are performed using VTRAN2 with a refined mesh to follow the waves of interest. Then the Kirchhoff method is used to examine the noise at the far-field. The viscous shock/boundary layer interaction is used, although the effect of this term is weak, as shown in reference [31].

We use a NACA 64A006 airfoil; the vortex strength was $C_{lv} = 0.4$ (C_{lv} is a nondimensional measure of the vortex strength: $C_{lv} = 2\Gamma/cU_o$) and the vortex miss-distance $y_o = -0.5$ chords, for a fixed vortex path. The initial vortex position is $x_o = -9.51$ chords and the free stream velocity is one (arbitrary units) so the vortex passes below the airfoil leading edge at time T = 9.51. The Mach numbers of 0.875, 0.854, and 0.822 correspond to shock wave motions of types A, B, and C, respectively, as also shown in references [9, 27]. The three different types of the unsteady shock motion are thus studied. For the Kirchhoff surface (figure 4) we used a span of 8 chords, $x_S = 0.25$ chords and $y_S = 3.5$, 2.5 and 1.9 chords for the three types A, B and C, respectively. y_S is chosen from figure 5, as explained before.

Initially, we run a couple of cases for verification purposes. Figure 7 shows the lift coefficient variation with instantaneous x-location of the vortex: VTRAN2 solution, NACA 64A006 airfoil, $M_\infty=0.85$, $\alpha = 0^o$, $C_{lv}=0.4$, and $y_o=-0.26$ chords. The result of the same for Euler solution can be found in reference [21]. The comparison shows that the two solutions are very close except the same difference on the trailing edge of airfoil, which is believed to be caused by the finer mesh is used by VTRAN2 on the trailing edge region. We also run the case: NACA0012 airfoil, $M_\infty=0.80$, $\alpha = 0^o$, $C_{lv}=0.4$, and $y_o=-0.26$. The comparison with Euler and Navier Stokes equations and other small disturbance formulations (from reference 56) is shown in figure 8 and is very satisfactory.

1. Noise Source Mechanisms of BVI

Figure 9 shows the $C_p(T)$ signal of the three types of unsteady shock motion in the far-field (point O, r=20 chords, $\theta=30^o$), as shown in figure 4, using Kirchhoff's method. The signal for the higher Mach number (type A) propagates upstream slower, so it takes a longer time to arrive at the same point. The signal consists of two disturbances (I, II) as also shown in references [27, 28]. The primary disturbance I is the main BVI noise and it originates at the airfoil when the vortex passes below the leading edge. The secondary disturbance II corresponds to the unsteady shock motion and depends on the motion of the shock wave, or even the entire supersonic region motion induced by the vortex passage. It originates at the airfoil at a later time, (when the vortex is 6-8 chords behind the airfoil), and depends heavily on the type of shock motion. The time delay of disturbance II decreases with decreasing Mach number and disappears in subcritical cases. The directivity of the two disturbances is very different as will be shown later. The existence of the second disturbance was observed computationally by George and Chang [6] and was also verified experimentally by Caradonna *et al.* [57] and Shenoy [58] and Lent *et al.* [59], and computationally by George and Lyrintzis [27, 28], Owen and Shenoy [22] and Liu *et al.* [26]. For example, Shenoy [58] performed some Schlieren experiments for a rotor and a second disturbance was seen to propagate in the far-field as postulated by computational results.

From figure 9 we can see that disturbance I increases slightly with increasing Mach number. We should also bear in mind that the definition of C_p includes division by M^2, so the effect of the Mach number is stronger than it appears in the above figures. Disturbance II also exists for type A and B shock motions, because it is caused by the movement of the entire supersonic pocket. It also appears to be decreasing as we move from type C to type A. However, if we measure it from peak to peak (instead of just reading the max value) it still increases, but at a lower rate than disturbance I.

Figure 10 shows the lift coefficient C_l (T) for a subcritical case (M=0.6) and types A, B and C of shock motion. We can see that the total change of C_l is higher at higher Mach numbers.

The drag coefficient C_d will be discussed next. It is well known that in uniform subcritical inviscid flow C_d is zero. It should be noted though, that C_d is not zero for subcritical inviscid BVI because of acceleration due to the vortex . When the flow becomes supercritical, the inviscid C_d is higher because of the formation of supersonic pockets. This was verified by running the code for subcritical and supercritical cases. C_d can be easily calculated in terms of the pressure distribution. Figure 11 shows C_d (T) for a subcritical case (M=0.6) and types A, B and C of shock motion. The change in the C_d signal is much lower than the change in the C_l. However, there is a significant increase as we move from subcritical to supercritical cases. Also the signal is positive when a shock wave is always present (e. g. type A). Finally, the C_d signal seems to catch some part of the second disturbance whereas C_l does not. This was also detected by Liu *et al.* [26] for some BVI cases using a thin layer Navier Stokes code, but is easier to see in the case of an oscillating flap [17], because there the periodicity of the motion is well-defined.

The directivity of the noise signal in the far-field is very complicated, as has been shown by experimental studies. Most of these experiments are also three-dimensional, which makes them very difficult to compare. For example, in reference 60 it was shown for a model helicopter rotor that the maximum signal can have a different direction if the advance ratio μ is varied.

Directivity is studied in a vortex (or fluid) fixed coordinate system keeping the distance from the vortex r_v constant (r_v = 50 chords). The relationship between the angles θ and θ_v in an airfoil fixed and a vortex fixed coordinate system is shown in figure 12. The observer is, however, fixed with the airfoil. Both ways of looking at the waves produced by BVI are effective in following the noise produced when the vortex meets the leading edge of the airfoil and, in principle, all their results can be transformed into each other. However, the second, fluid-fixed way is not as effective in following any waves which originate at the airfoil when the vortex has been convected a chord length or more behind the airfoil. Such waves typically are associated with unsteady shock motion on the airfoil, which typically originates when the vortex is 6 to 8 chord lengths behind the airfoil. The vortex-oriented, or fluid-fixed, viewpoint is closer to the case of a helicopter flyover. However, forward-radiated disturbances in the mid-field which are emitted at times after the vortex passage are sometimes difficult to observe. Some further discussion on the coordinate systems can be found in reference [27].

The Cp(t) signal for different directions is plotted in figures 12 and 13 for a subcritical case (M=0.6) and type C shock motion, respectively (note that span = 4 chords for this case). From figure 12 (M=0.6) we can see that we have only one disturbance. The amplitude of that disturbance is increasing as the direction angle θ increases from 0^o to 90^o (downward directivity). In figure 13 we can see two disturbances. Disturbance I is getting weaker as the direction angle θ increases from 0^o to 90^o (forward directivity). Disturbance II is getting stronger as the direction angle θ increases from 0^o to 90^o (downward directivity). The two disturbances also move closer as the angle θ is increased, and finally almost merge at $\theta = 120^o$. This implies a different point of origin.

In figures 12 and 13 the observer is still fixed with respect to the airfoil. The observer can be easily made to move with the vortex, as is implied by the use of the vortex-fixed coordinate system. If we do that, the results for type C are shown in figure 14. The BVI signals are slightly modified. For example, for $\theta=30^o$ ($\theta v=5.73^o$) the second disturbance is larger and is closer to the first one, because the observer is moving closer to the airfoil after the first disturbance. (If the second disturbance is emitted when the vortex is 7 chordlengths downstream, then with moving observer θ is increased to 76.8^o and r is almost half.) Figure 15 shows frequency spectra for the

above case with moving observer using Fast Fourier Transform (FFT). However, these results do not seem to be very accurate probably due to descretization errors. Since in most experiments a vortex-fixed coordinate system is used, a moving observer should be used for verification of future experimental results.

We propose to regard the noise due to transonic BVI as being composed of the following two parts: (1) linear acoustic source (dipole); (2) non-linear acoustic source (quadrupole).

The linear acoustic source, is associated with oscillating drag and lift, C_l and C_d signals as shown in figures 10 and 11, and the corresponding noise directivity presents dipole patterns in the same way as does linear acoustic analysis. This behavior can be observed if we look at the subsonic case (e. g. M=0.6) directivity in figure 12. In this case there is only disturbance I which has a downward directivity, since the C_l variation is much stronger than the C_d, it is expected that the C_l does dominate the linear signal.

The non-linear acoustic source is related to the shock wave variations on the airfoil lower surface during a BVI. The noise is related to shock strength variations and the amplitude of the shock wave motion. Shock strength variations occur as the vortex passes below the airfoil and can be detected by the significant increase in the C_d signal for the supercritical cases. They generate a strong portion of disturbance I that dominates the signals, especially at the horizontal direction and has a C_d dipole directivity. Thus we can see from figure 13, which shows the directivity of the type C shock motion, that disturbance I now has a forward directivity. Abrupt shock wave motions cause variations of the entire supersonic pocket. These variations usually take place much later and generate disturbance II, which can also be detected from the C_d signal. Disturbance II has a more complicated directivity. Trying different Mach numbers and different airfoil shapes (see for example reference 31), we found that disturbance II becomes maximum at an an angle between 60^o and 90^o, depending on the flow parameters.

Thus, disturbance I depends on the shock strength and the C_l variations as the vortex passes below the airfoil. In subcritical cases only the C_l variations are relevant, and in supercritical cases the shock noise dominates, especially near the horizontal. Disturbance II depends on the shock motion that is generated when the vortex is farther downstream (6-8 chords). The two disturbances can have a different point of origin, which changes their relative distance, as shown in figure 13. Disturbance I can be reduced by weakening the shock formation on airfoil, and disturbance II can be reduced by stabilizing the shock wave motion on airfoil.

3. Some Cases for Future BVI Experiments

Some test cases for future BVI experiments are shown here. For all test cases we have a NACA 0012 airfoil, vortex strength C_{lv}=0.65, a fixed vortex path, initial vortex position -9.51 chords. The cases are:

Case 1: M=0.70, y_o=-0.26, $\alpha=0^o$

Case 2: M=0.71, y_o=-0.26, $\alpha=0^o$

Case 3: M=0.70, y_o=-0.26, α= 0.2345^o (corresponding C_l without a vortex=0.04)

Case 4: M=0.70, y_o=-0.26, α= -0.2345^o (corresponding C_l without a vortex=-0.04)

For all the cases C_l, C_d, and far-field directivity signals are shown in figures 16-26. From figure 16 we can see that the slight increase for the Mach number between cases 1 and does not influence C_l and C_d very much. Directivity signals (figures 17-20) for both fixed and moving observer show that the signal is max when θ is between 60^o and 70^o which corresponds to $\theta_v=22^o$-28^o. Finally (as will also be shown in section 4c of the results) for cases 3 and 4 we can see from

figures 21-26, that an increase of the angle of attack (i. e. from 0 to 0.2345) decreases the resulting BVI noise, whereas a decrease in the angle of attack increases the resulting BVI noise. From figures 23-26 we can see that the directivity patterns remain almost unchanged.

4. Noise Reduction Techniques

Several ideas for noise reduction of transonic BVI are introduced as follows:

a) Airfoil shape modifications:

The transonic BVI shock motions are mainly generated on the lower airfoil surface. Thus the lower surface of the airfoil needs to be modified, particularly near the leading edge, because disturbance I is generated as the vortex passes below the airfoil leading edge and disturbance II depends on the shock wave motion which is influenced by changes near the leading edge. Initially, as a theoretical test, we used a simple cosine function (1-cosx) as the shape added to a section of the airfoil (NACA64A006) that gives the continuous slope for the modified airfoil. Then the more practical NACA 4-digit airfoil shape is added to the airfoil.

Figure 27 shows the modified airfoil shape in comparison with original one. The maximum thickness added is 0.4% and 0.8% and the total distance of the modification is 38% from leading edge. It should noted here that all shapes are shown three times fatter, so that the modification can be detected easier. The 0.8% modified airfoil was given a small angle of attack $\alpha=0.028^o$, so that the C_l stays the same, but our conclusions are also valid at $\alpha=0^o$. The 0.4% modified airfoil was run at $\alpha=0^o$, since the changes in the C_l are very small in this case. Figure 27 shows the corresponding far-field noise signals at $\theta=30^o$ and $\theta=90^o$. We can see from these figures that both disturbances are reduced. However, another small disturbance is generated in between, and is mainly due to shape irregularities near the end of the modification interval. The 0.4% modification produces less noise.

Then we moved the modification interval from 38% to 26%, and used the smaller maximum thickness (i. e. 0.4%). Figure 28 shows the modified airfoil and the corresponding far-field noise signals at $\theta=30^o$ and $\theta=90^o$. The 38% modification is also included in the figure for comparison purposes. We can see that the 26% modification interval gives somewhat better results.

We also modified the airfoil by adding a NACA 4-digit thickness line, with the same maximum thickness as before (i. e. 0.4%) on 38% region of the airfoil. The disadvantage of adding such a shape is that the slope of the airfoil surface is no longer continuous. Figure 29 shows the airfoil modification and the corresponding far-field noise signals at $\theta=30^o$ and $\theta=90^o$, respectively. For this case, we used the angle of attack $\alpha=.04^o$ in order to get same lift with the unmodified airfoil. In comparison with result from cosine modification, disturbance II decreased substantially, which means that the shock motion was stabilized to some degree. The additional small disturbance that appeared in the previous cosine-shaped modification has almost disappeared. From figure 29 we can see that the NACA 4-digit shape produces less noise than the cosine-shaped modification.

The above results showed us that a small (e. g. 0.4% maximum thickness) modification close to the leading edge (e. g. 25% modification section) can lower substantially the BVI noise. The shape of the modification is important and should be adjusted using trial and error, so that aerodynamic performance does not deteriorate.

A modified airfoil SC1095rn was developed by Sikorsky Aircraft Co. to improve the aerodynamic characteristics of the SC1095 airfoil. Figures 30-32 show the time history of the C_l and C_d with the comparison between airfoils SC1095 and SC1095rn for the cases of free stream Mach number M_∞=0.6, 0.7, and 0.8 accordingly. For all cases, the vortex strength was C_{lv}=0.4 the vortex miss-distance y_0=-0.5 chords, for a fixed vortex path, the initial vortex position is -9.51 chords. The following things should be noted that there are two pulses found in $C_d(T)$ and one pulse in $C_l(T)$, as in previous cases. The pulses for SC1095rn seemed to appear weaker than the ones for SC 1095, especially when the Mach number increases from M_∞=0.6 to 0.8. As the free steam velocity increase, the second pulse in $C_d(T)$ becomes stronger, which is because stronger shock waves are being generated.

The corresponding far-field acoustic signal $C_p(T)$ is shown in figures 33-37 at 30° below the airfoil. The first pulse in $C_p(T)$, the difference between SC1095 and SC1095rn airfoils remains about the same when the free stream Mach number increases from M_∞=0.6 to 0.8, and the pulse for SC1095 is stronger. This could be because SC1095rn airfoil enlarges the radius of leading edge which reduces the effects of the vortex passage. The second pulse, is stronger for SC1095 compared to SC1095rn and the difference increases when the free stream Mach number increases from M_∞=0.6 to 0.8. It is believed that this increase is related to the shock wave which is generated on the airfoil lower surface. The shock wave generated in SC1095rn is stronger, but it does not move as much, generating less noise.

The corresponding far-field directivity of the acoustic signals showed in figures 38-43, for a fixed observer. For M_∞=0.6, the first pulse reaches the maximum value at θ=90°, and there are no significant differences between the directivity for SC1095 and SC1095rn airfoil. Starting from M_∞=0.7, there are two pulses appeared in the far-field directivity acoustic signals. The first pulse reaches the maximum value at θ=0° and the second pulse reaches its maximum value at θ=70°, while the two pulses become equally significant at θ=30°, starting at M_∞=0.7 to 0.8. In general, the noise directivity patterns are the same between the two airfoil, but the pulse amplitudes for SC1095 are stronger than the ones for SC1095rn and the differences increase when free stream Mach number increases from M_∞=0.6 to 0.8. As a concluding remark we can say that, although SC1095rn airfoil was developed to improve aerodynamics, it also generated less far-field BVI noise.

Finally, from a study of 4-digit NACA airfoil shapes we found [31] that symmetric airfoils, and airfoils with a point of maximum camber further upstream, seem to give less BVI noise for conditions producing the same lift.

b) Splitting one vortex into two vortices:

This idea can be realized by splitting the trailing vortex using a small airfoil slat in front of the main airfoil. Some exploratory experiments [61] are currently conducted with such a configuration. Figure 44 shows the idea behind the two-vortex model. In order to simplify the problem we have assumed that the distance between the vortices remains constant. Figure 44 also shows the effect of splitting the vortex in BVI far-field noise. We varied the distance between the two vortices from d=.25 to .5. It is shown from figure 44 that the longer the distance between the splitting vortices, the more the noise can be reduced, although the noise is not reduced as much as with airfoil shape modification.

c) Changing Other Parameters

The vortex strength is a very important parameter. If we can reduce the vortex strength by one half by designing a better blade tip, for example, then the corresponding far-field noise will be reduced greatly as shown in figure 45. However, the vortex miss distance does not have a very strong effect (for distances 0.25 to 0.5 chords), as shown elsewhere [28].

When we want larger lift (thrust), the angle of attack should be increased. In such case, figure 46 shows one example where both disturbances are reduced significantly. This explains why the maximum BVI noise always occurs in a certain helicopter descent region. BVI noise can be reduced by a proper combination of advance ratio and descent rate during approach into a noise sensitive area (Schmitz and Yu [5]).

Conclusions

An existing numerical finite difference code VTRAN2 was used to analyze noise due to transonic BVI. The two-dimensional unsteady transonic small disturbance equation was solved numerically using ADI techniques with monotone switches, including viscous effects due to shock-boundary interactions and the cloud-in-cell method for the simulation of the vortex. The Kirchhoff's method was used to extend the numerically calculated two-dimensional near-field aerodynamic results to the three-dimensional linear acoustic far-field.

The effect of the three types of unsteady shock motion (A, B and C) was investigated. The unsteady pressure coefficients $C_p(t)$ showed the existence of two main disturbances. The first one (I) is believed to be associated with the fluctuating lift coefficient (C_l) (linear noise) and the shock strength variations generated when the vortex passes below the airfoil (nonlinear noise); disturbance I has a strong forward directivity. The second (II) is believed to be associated with the movement of the shock wave generated at a later time (the vortex is 6-8 chordlengths behind the airfoil) and has a strong downward directivity (nonlinear noise). The maximum radiation occurs at an angle θ between 60^o and 90^o below the horizontal for an airfoil-fixed coordinate system; it depends on both disturbances I and II and the details of the airfoil shape.

Modified airfoil designs can be very effective in reducing the BVI noise under the same lift and Mach number conditions. In particular, a small (e. g. 0.4% maximum thickness) modification close to the leading edge (e. g. 25% modification section) can lower substantially the BVI noise. The overall BVI noise can be reduced by utilizing the modified airfoil SC1095rn in comparison with airfoil SC1095, especially for the higher Mach number cases. Thus, although SC1095rn airfoil was developed to improve aerodynamics, it also reduced the BVI noise. Experiments should be conducted to verify the prediction, as well as to cover evaluation of other noise source effects. The shape of the modification is also very important, and should be investigated further.

It was shown that splitting the vortex into two can reduce the noise significantly. In fact, both disturbances are reduced. Also, the longer the distance between the two vortices the lower will be the noise produced. It is shown that BVI noise will be greatly reduced by reducing the vortex strength which can be achieved with a better blade tip design. Also, BVI noise will be greatly reduced by increasing the angle of the attack, which it explains why thrust can have an effect on BVI noise. BVI noise can be reduced by a proper combination of advance ratio and descent rate during approach into a noise sensitive area.

Acknowledgements

C. Kitaplioglu from NASA Ames Research Center was the technical monitor and his suggestions during the course of the research are greatly appreciated by the authors. The calculations were performed at the computational facilities of Minnesota Supercomputer Institute (MSI).

References

1. Johnson, W. R., "Recent Developments in Rotary-Wing Aerodynamic Theory," *AIAA Journal*, Vol. 24, No. 8, Aug. 1986.

2. Bries, E., Barbini, W., and Honaker J., "Current Issues Affecting the Civil Industry" *Vertiflite Journal*, Jan. 1991 pp. 20-23.

3. George, A. R., "Helicopter Noise: State-of-the-Art," *Journal Aircraft*, Vol. 15, No. 11, November 1978, pp. 707-715.

4. Schlinker, R. H., and Amiet, R. K., "Rotor-Vortex Interaction Noise," NASA CR-3744, Oct. 1983.

5. Schmitz, F. H., and Yu, Y. H., "Helicopter Impulsive Noise: Theoretical and Experimental Status," in *Recent Advances in Aeroacoustics*, A. Krothapalli and C. A. Smith, editors, Springer-Verlag, NY, 1986.

6. George, A. R., Smith, C. A., Maisel, M. D. and Brieger, J. T., "Tilt Rotor Aircraft Aeroacoustics,"*Proceedings of the 45th Annual Forum of the American Helicopter Society*, Boston, MA., May 1989.

7. Poling, D. R., Dadone, L., Telionis, D. P., "Blade-Vortex Interaction," *AIAA Journal*, Vol. 27, No. 6, June 1989, pp. 694-699.

8. George, A. R. and Chang, S. B., "Noise Due to Transonic Blade-Vortex Interactions," *Proceedings of the 39th Annual National Forum of the American Helicopter Society*, Paper A-83-39-50-D000, 1983.

9. George, A. R. and Chang, S. B., "Flow Field and Acoustics of Two-dimensional Transonic Blade-Vortex Interactions," AIAA Paper 84-2309, AIAA 9th Aeroacoustics Conference, Williamsburg, VA, October 15-17, 1984.

10. Ballhaus, W. F. and Goorjian P. M. "Implicit Finite-Difference Computations of Unsteady Transonic Flows about Airfoil," *AIAA Journal.*, Vol. 15, No. 12, Dec. 1977, pp. 1728-1735.

11. Rizzetta D. P., and Chin, W. C., "Effect of Frequency in Unsteady Transonic Flow," *AIAA Journal*, Vol. 17, No. 7, July 1979, pp. 779-781.

12. Guruswamy P. and Goorjian P. M."Effects of Viscosity on Transonic Aerodynamic and Aeroelastic Characteristics of Oscillating Airfoils" *AIAA Journal*, Vol. 21, No. 9, Sept. 1984, pp. 700-707.

13. Goorjian, P. M., Meagher, M. E., and Van Buskirk, R. D., "Monotone Switches in Implicit Algorithms for Potential Equations Applied to Transonic Flows" *AIAA Journal*, Vol 23, No. 4, Apr. 1985, pp. 492-498.

14. Goorjian, P. M., and Van Buskirk, R. D., "Second-Order-Accurate Spatial Differencing for the Transonic Small-Disturbance Equation" *AIAA Journal*, Vol. 23, No. 11, Nov. 1985, pp. 1693-1699.

15. Lyrintzis, A. S., and George, A. R., "VTRAN2: Computation of Two-dimensional Blade-Vortex Interactions Using the Unsteady Small Disturbance Equation, (User's Manual)" Cornell University, Ithaca NY, March 1986.

16. Lyrintzis, A. S. "Transonic Blade-Vortex Interactions," Ph.D. Dissertation, Mechanical and Aerospace Engineering Department, Cornell University, Ithaca NY, Jan. 1988.

17. Lyrintzis, A. S., and Xue, Y., "Acoustics of Transonic Flow Around an Oscillating Flap," to appear in *Journal of Fluids Engineering;* also University of Minnesota Supercomputer Institute Research Report, UMSI 91/169, Minneapolis, MN, June 1991.

18. McCroskey, W. J. and Goorjian, P. M., "Interactions of Airfoils with Gusts and Concentrated Vortices in Unsteady Transonic Flow," AIAA Paper 83-1691, AIAA 16th Fluid and Plasma Dynamics Conference, Danvers, MA, July 1983.

19. Srinivasan, G. R., McCroskey, W. J., and Kutler, P., "Numerical Simulation of the Interaction of a Vortex with Stationary Airfoil in Transonic Flow," AIAA Paper 84-0254, AIAA 22nd Aerospace Sciences Meeting, Reno, Nevada, Jan., 1984.

20. Sankar, N. L., and Tang, W., "Numerical Solution of Unsteady Viscous Flow Past Rotor Sections," AIAA Paper 85-129, Jan. 1985.

21. Srinivasan, G. R., McCroskey, W. J., and Baeder J. D., "Aerodynamics of two-dimensional Blade-Vortex Interaction," *AIAA Journal*, Vol. 24 No. 10, Oct. 1986, pp. 1569-1576.

22. Owen S. T., and Shenoy R. K., "Numerical Investigation of Two-Dimensional Blade-Vortex Interaction," *Proceedings of the AHS National Specialists' Meeting on Aerodynamics and Aeroacoustics*, Arlington, Texas, Feb. 1987.

23. Damodaran, M., and Caughey, D. A., "A Finite Volume Euler Calculation of the Aerodynamics of Transonic Airfoil-Vortex Interaction," *AIAA Journal*, Vol. 26, No. 11, Nov. 1988, pp.1346-1353.

24. Baeder, J. D., McCroskey, W. J., and Srinivasan, G. R., "Acoustic Propagation Using Computational Fluid Dynamics," *Proceedings of the 42nd Annual Forum of the American Helicopter Society,* Washington, DC, June, 1986, Vol.1, pp. 551-562.

25. Baeder, J. D., "Computation of Non-Linear Acoustics in Two-Dimensional Blade-Vortex Interactions," 13th European Rotorcraft Forum, Arles, France, Sept. 1987.

26. Liu, N. S. Davoudzadeh, F., Briley, W. R., and Shamroth, S. J., "Navier Stokes Simulation of Transonic Blade-Vortex Interactions," *Proceedings of the International Symposium on Nonsteady Fluid Dynamics (ASME)*, Miller, J. A., and Telionis, D. P., editors, Toronto, Canada, June 1990, pp 177-186.

27. George, A. R., and Lyrintzis, A. S., "Acoustics of Transonic Blade-Vortex Interactions," *AIAA Journal*, Vol. 26, No. 7, July 1988, pp. 769-776.

28. Lyrintzis, A. S., and George, A. R., "Far-Field Noise of Transonic Blade-Vortex Interactions," *American Helicopter Society Journal*, Vol. 34, No.3, July 1989, pp.30-39.

29. Lyrintzis, A. S., and George, A. R., "The Use of Kirchhoff Method in Acoustics," *AIAA Journal*, Vol. 27, No. 10, Oct. 1989, pp. 1451-1453.

30. Lyrintzis, A. S., and George, A. R., "Study of Transonic Blade-Vortex Interaction Noise,"*Noise Control Engineering Journal*, Vol. 32, No. 3, May-June 1989, pp.105-109.

31. Lyrintzis, A. S., and Xue, Y., "A Study of the Noise Mechanisms of Transonic Blade-Vortex Interactions", to appear in Oct. 1991 issue of *AIAA Journal;* also University of Minnesota Supercomputer Institute Research Report, UMSI 90/141, Minneapolis, MN, July 1990.

32. Xue, Y., and Lyrintzis, A. S., "Noise Reduction for Transonic Blade-Vortex Interactions," to be presented at the American Helicopter Technical Specialists meeting on Rotorcraft Acoustics and Fluid Dynamics, Philadelphia, PA, Oct. 1991; also University of Minnesota Supercomputer Institute Research Report, UMSI 91/205, Minneapolis, MN, August 1991.

33. Ballhaus, W. F., "Some Recent Progress in Transonic Flow Computations," in *Numerical Methods in Fluid Dynamics*, ed. Wirz H. J., and Smolderen J. J., McGraw Hill, NY 1978, pp. 155-235.

34. Rizzetta, D. P., "Procedures for the Computation of Unsteady Transonic Flow Including Viscous Effects," NASA CR-166249, 1982.

35. Poling, D. R., Telionis, D. P., "The Response of Airfoils to Periodic Disturbances-The Unsteady Kutta Condition," *AIAA Journal*, Vol.24, No.2, Feb. 1986, pp. 193-199.

36. Chang, S. B., "Aerodynamics and Acoustics of Transonic Two-Dimensional Blade-Vortex Interactions," Ph.D. Dissertation, Mechanical and Aerospace Engineering Department, Cornell University, Ithaca NY, Jan. 1985.

37. Tadghighi, H., Hassan, A. A., and Charles, B., "Prediction of Blade-Vortex Interaction Noise Using Airloads Generated by a Finite-Difference Technique," *Proceedings of the 46th Annual Forum of the American Helicopter Society*, Washington DC, May 1990, Vol. I, pp. 367-378.

38. George, A. R., "Noise from High Speed Surfaces," in Aero- and Hydro-Acoustics IUTAM Symposium Lyon 1985, G. Compte-Bellot and J. E. Ffowcs Williams editors, Springer, Berlin, Heidelberg 1986.

39. Farassat, F., and Brentner, K. S., "The Uses and Abuses of the Acoustic Analogy in Helicopter Rotor Prediction," *Proceedings of the American Helicopter Society National Specialists' Meeting on Aerodynamics and Aeroacoustics,* Arlington, TX, Feb. 1987.

40. Morgans, R. P., "The Kirchhoff Formula Extended to a Moving Surface," Philosophical Magazine, 9, s.7, No. 55, 1930, pp. 141-161.

41. Hawkings, D. L., "Noise Generation by Transonic Open Rotors," Westland Research Paper 599, 1979.

42. Morino, L., "A General Theory of Unsteady Compressible Potential Aerodynamics," NASA Contractor Report CR-2464, December 1974.

43. Morino, L., "Steady, Oscillatory, and Unsteady Subsonic and Supersonic Aerodynamics - Production Version 1.1 (SOUSSA-P, 1.1), Vol. 1, Theoretical Manual," NASA Contractor Report CR-159130, 1980.

44. Morino, L., "Mathematical Foundations of Integral Methods," in Computational Methods in Potential Aerodynamics, Morino L. editor, Springer-Verlag, 1985, pp. 270-291.

45. Farassat, F., and Myers, M. K., "Extension of Kirchhoff's Formula to Radiation from Moving Surfaces," *Journal of Sound and Vibration*, Vol. 123, No. 3, June 1988, pp.451-460.

46. Jones, D. S., *The Theory of Electromagnetism*, Pergamon Press, 1964.

47. Stratton, J. A., *Electromagnetic Theory*, McGraw-Hill, 1941.

48. Pierce, A. D., *Acoustics-An Introduction to its Physical Principles and Applications*, New York, McGraw-Hill, 1941.

49. Forsyth, D. W., and Korkan, K. D., "Computational Aeroacoustics of Propeller Noise in the Near- and the Far-field," AIAA paper 87-0254, AIAA 25th Aerospace Science Meeting Reno, Nevada, Jan. 1987.

50. Jaeger, S., and Korkan, K. D., "On the Prediction of Far-Field Computational Aeroacoustics of Advanced Propellers," AIAA paper 90-3996, AIAA 13th Aeroacoustics Conference, Oct. 1990.

51. Purcell, T. W., Strawn, R. C., and Yu, Y. H., "Prediction of High-Speed Rotor Noise With a Kirchhoff Formula," Proceedings of the American Helicopter Society National Specialists' Meeting on Aerodynamics and Aeroacoustics, Arlington, TX, Feb. 1987.

52. Purcell, T. W., "CFD and Transonic Helicopter Sound," Paper No. 2, 14th European Rotorcraft Forum, Sept. 1988.

53. Baeder, J. D., "Euler Solutions to Nonlinear Acoustics of Non-Lifting Hovering Rotor Blades," 16th European Rotorcraft Forum, Glascow, Scotland, Sept. 1990.

54. Tijdeman, H., "Investigations of the Transonic Flow Around Oscillating Airfoils," NLR TR 77090- U, NLR The Netherlands, 1977.

55. Tangler, J. L., "Schlieren and Noise Studies of Rotors in Forward Flight," Paper 77, 33-05, Presented at the 33rd Annual National Forum of the American Helicopter Society, Washington, D. C., May 1977.

56. Baeder, J. D., "The Computation and Analysis of Acoustic Waves in Transonic Airfoil-Vortex Interactions", Ph.D. Dissertation, Dept. of Aeronautical and Astronautical Engineering, Stanford University, Sept. 1989.

57. Caradonna, F. X., Laub, G. H., and Tung, C., "An Experimental investigation of the Parallel Blade-Vortex Interaction," 10th European Rotorcraft Forum, The Hague, Netherlands, August 1984.

58. Shenoy, R. K. "Aeroacoustic Flowfield and Acoustics of a Model Helicopter Tail Rotor at a High Advance Ratio," *Proceedings of the 45th Annual Forum of the American Helicopter Society*, Boston, MA., May 1989.

59. Lent, K., Lohr, K., Meier, G., Miller, K., Schievelbusch, O., Schurmann O., and Szumowski, A., "Noise Mechanisms of Transonic Blade-Vortex Interaction," AIAA paper 90-3972, AIAA 13th Aeroacoustics Conference, Oct. 1990.

60. Martin, M. R., and Splettstoesser, W. R., "Acoustic Results of the Blade-Vortex Interaction Acoustic Test of a 40 Percent Model Rotor in the DMW," *Proceedings of the American Helicopter Society National Specialists' Meeting on Aerodynamics and Aeroacoustics*, Arlington, Texas, Feb. 1987.

61. Telionis, D. P., private communication.

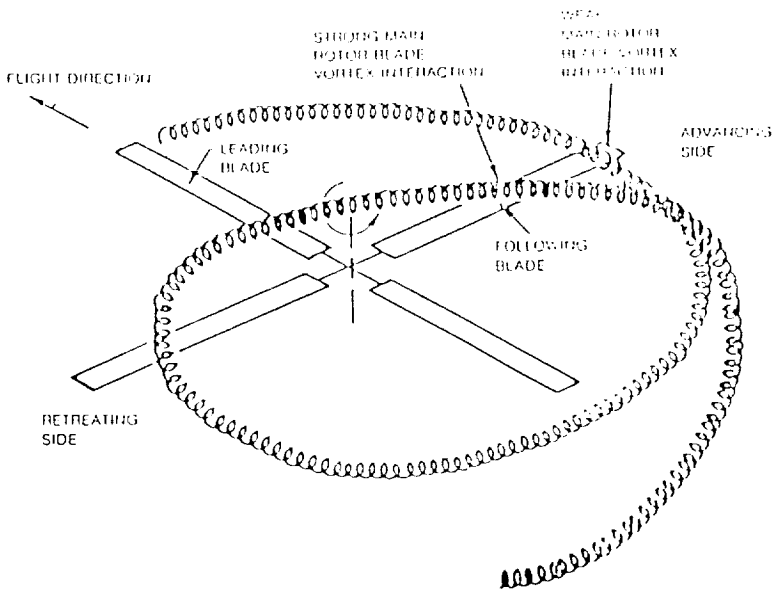

Figure 1. Formulation of BVI for a four blade rotor (from Schlinker and Amiet [4]).

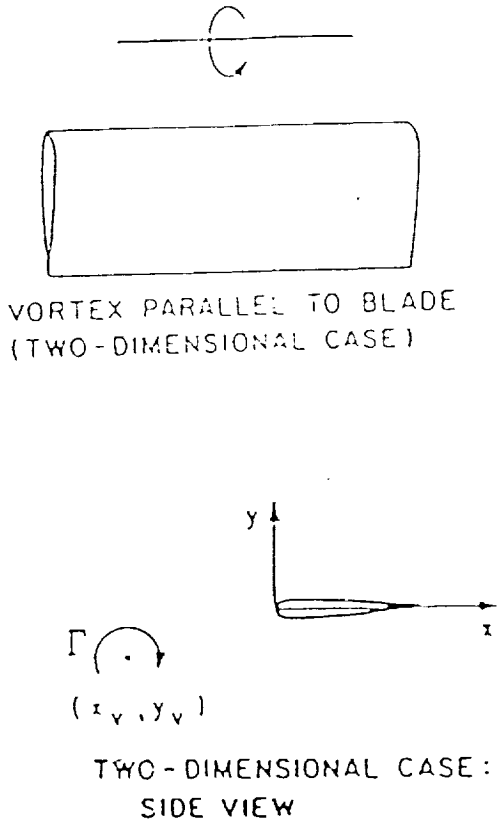

Figure 2. Two-dimensional BVI.

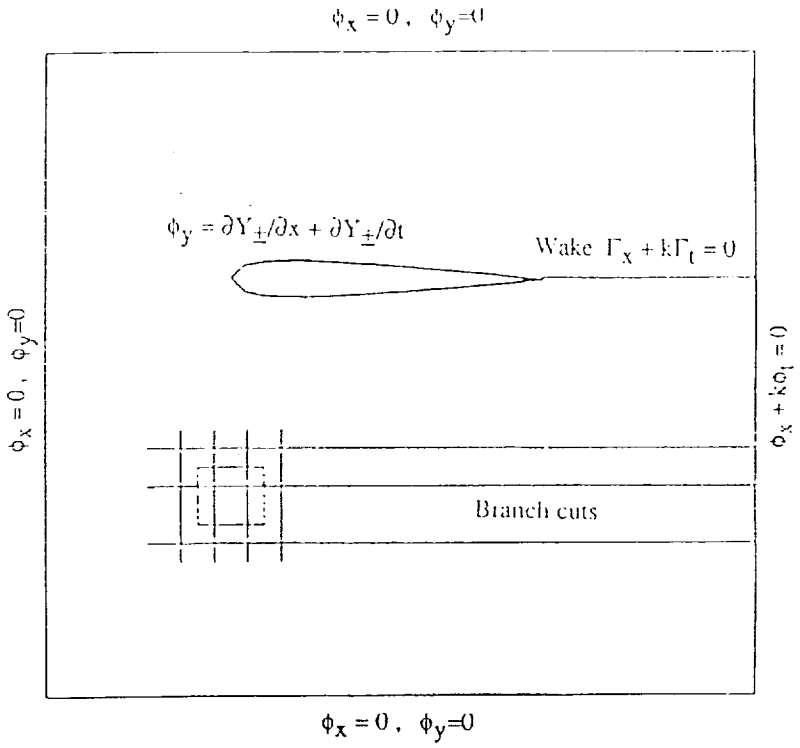

Figure 3. Domain and boundary conditions for VTRAN2.

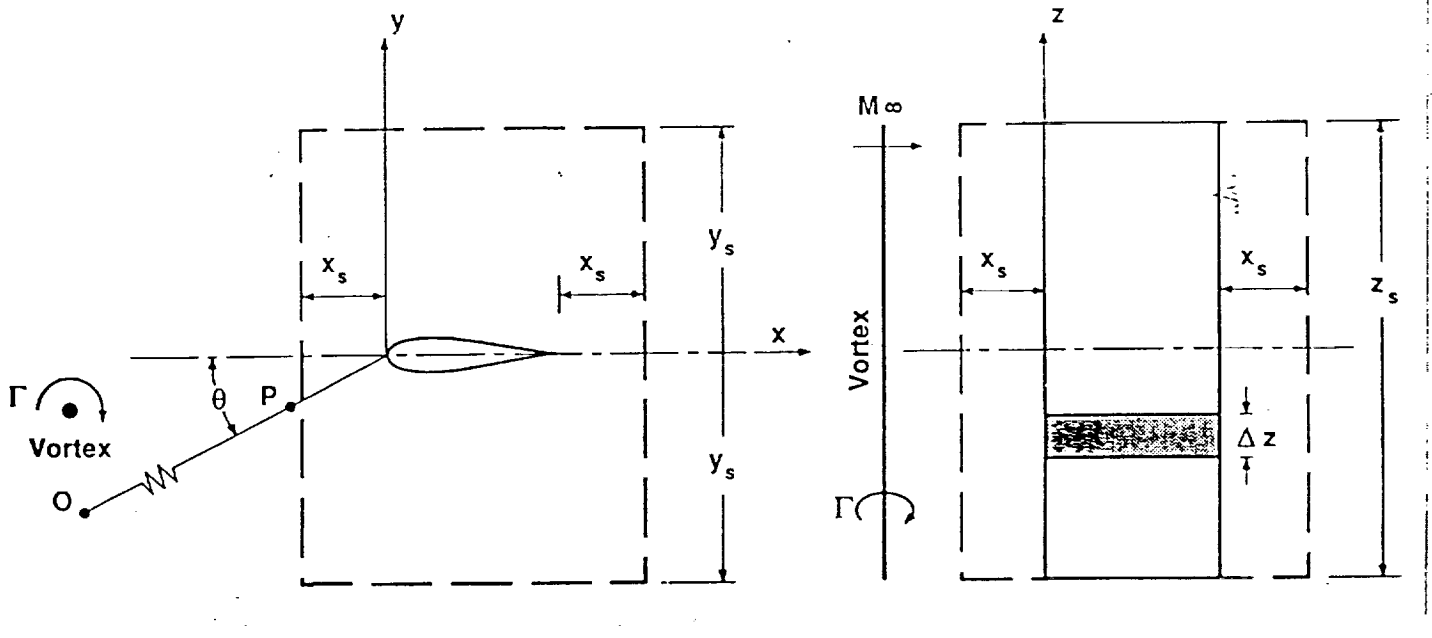

Figure 4. Kirchhoff's surface for the calculation of the far-field.

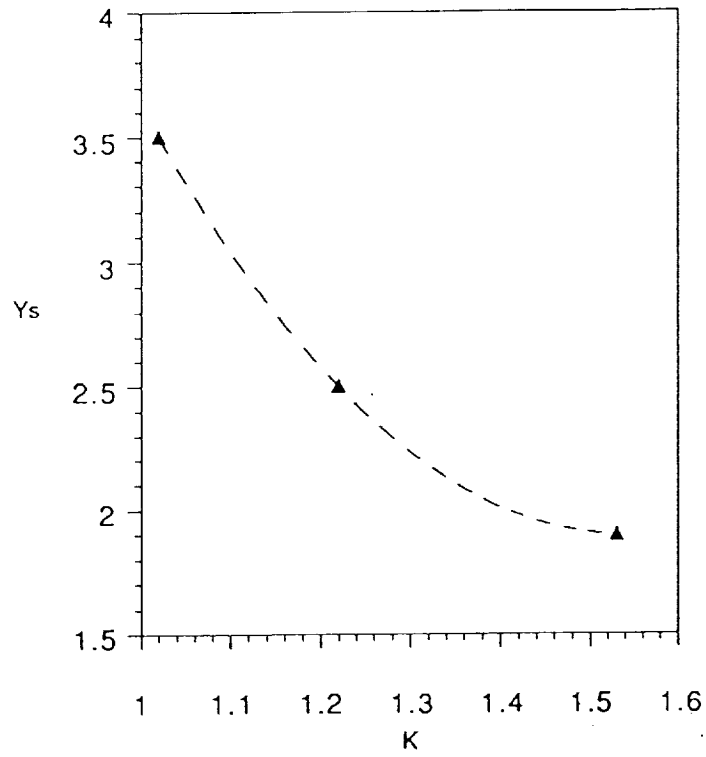

Figure 5. Empirical relationship of Kirchhoff surface length y_s vs transonic similarity parameter K.

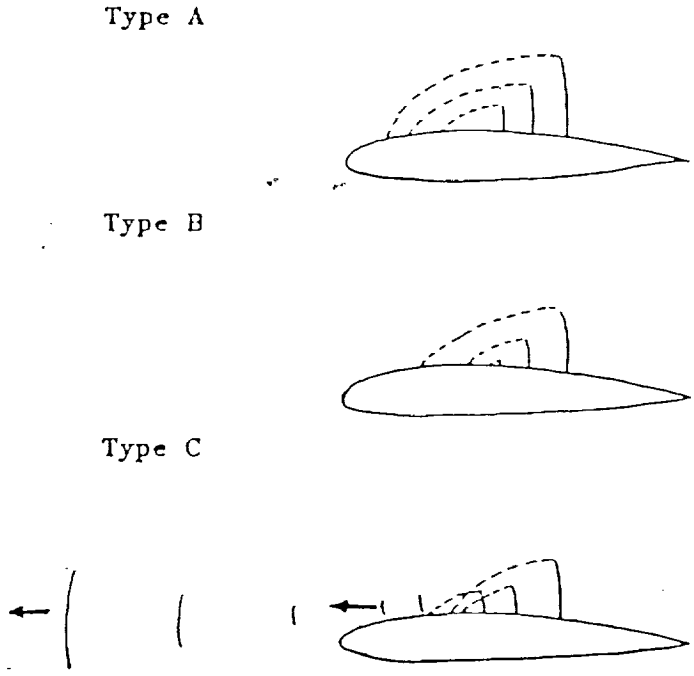

Figure 6. The three types of unsteady shock motion.

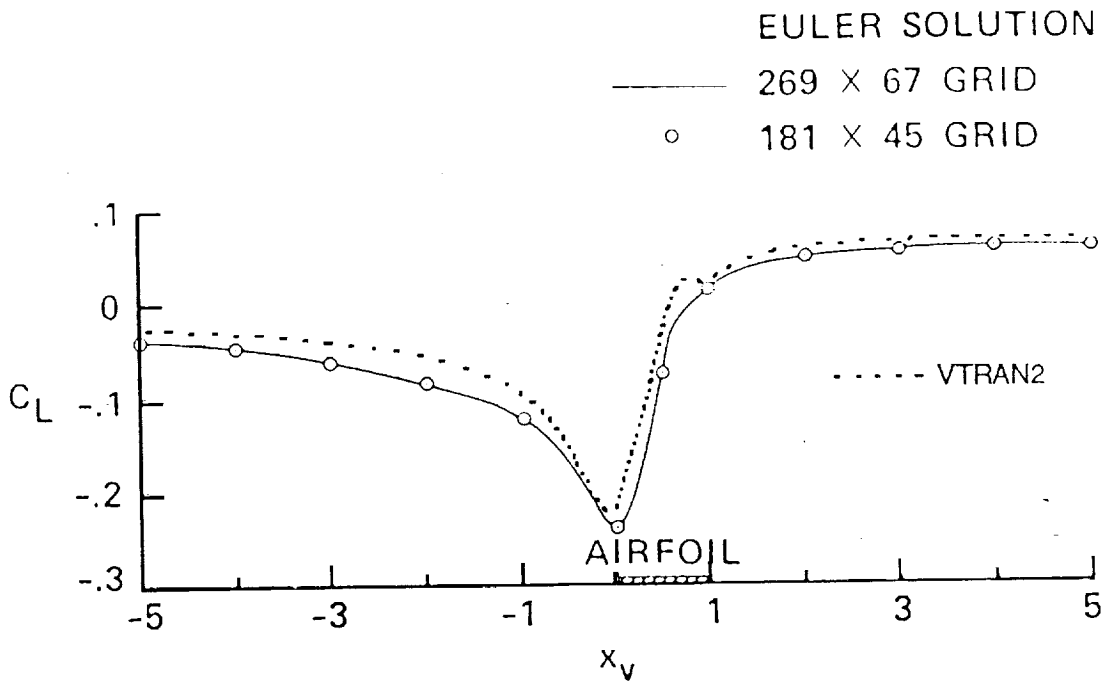

Figure 7. Comparison of VTRAN2 with Euler solution (from [21]); 64A006, M=0.85, C_{lv}=0.4, y_o=-0.26.

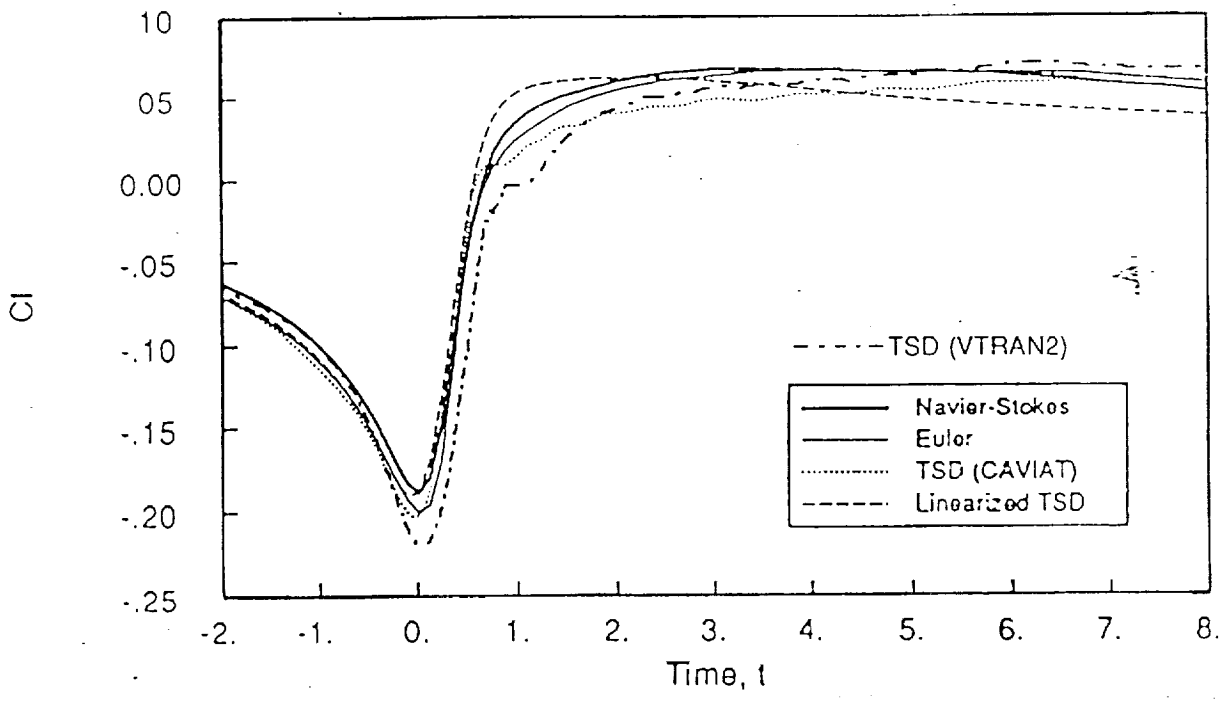

Figure 8. Comparison of VTRAN2 results with other codes (from [56]); 0012, M=0.8, C_{lv}=0.4, y_o=-0.26.

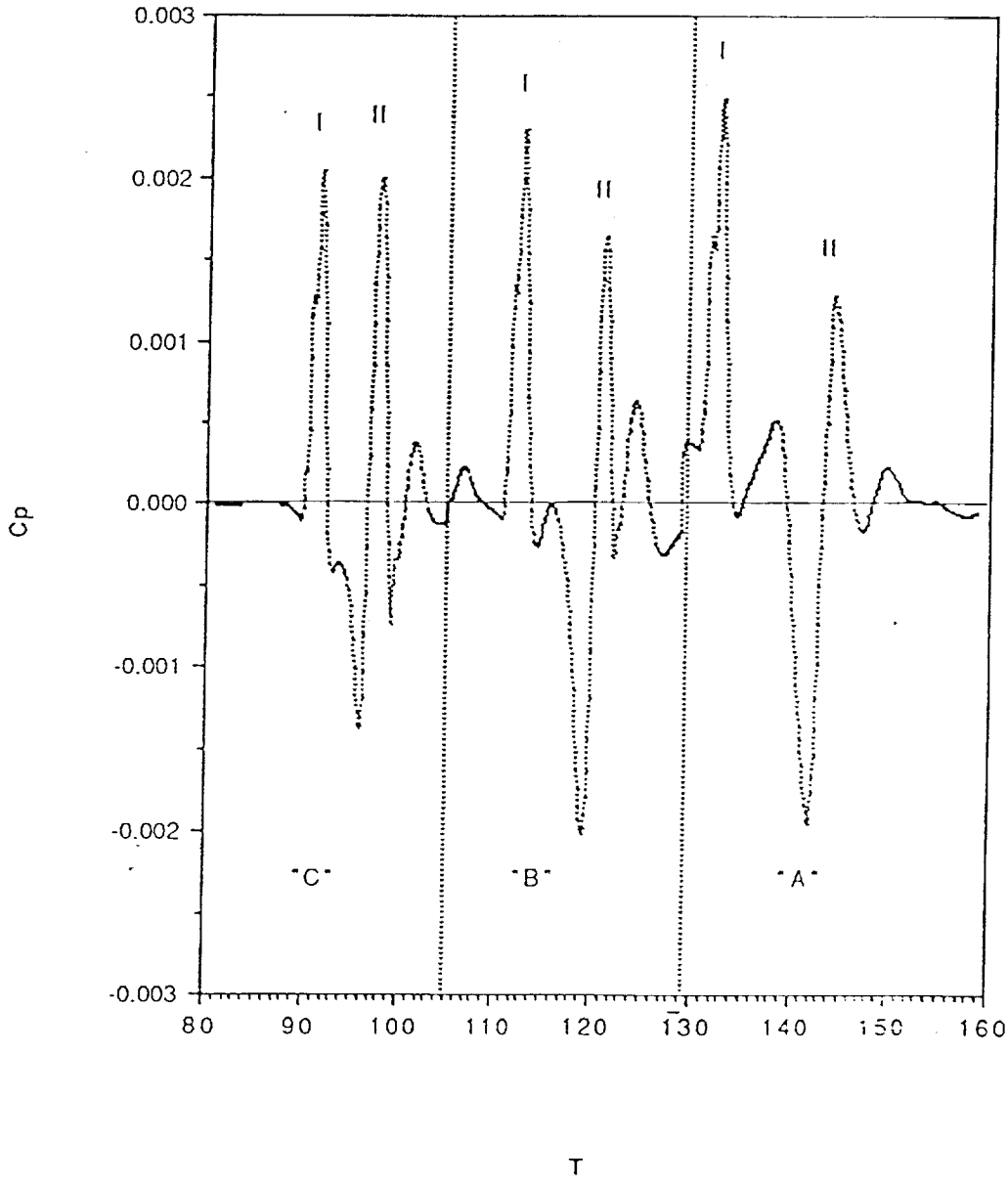

Figure 9. Comparison of the far-field BVI noise for types A, B, C; point O (r = 20 chords, θ=30°, span = 8 chords).

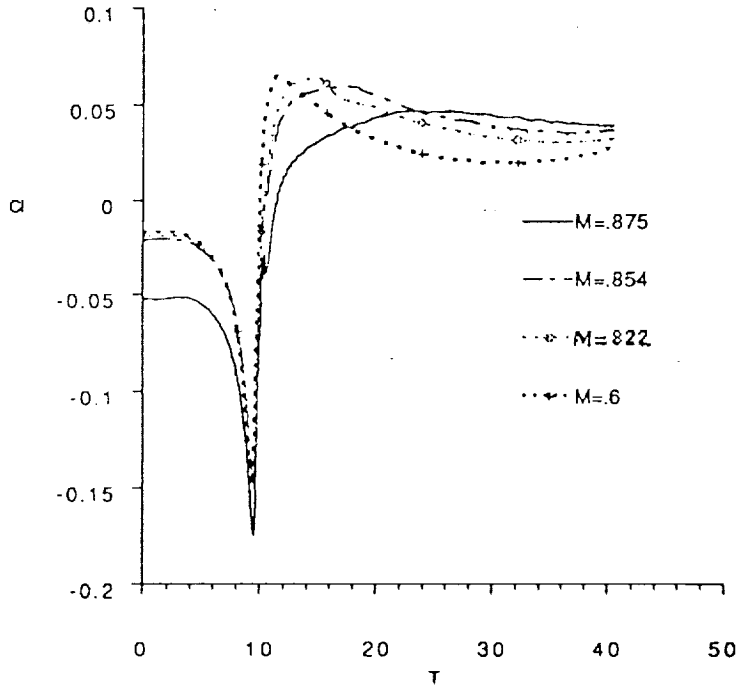

Figure 10. Comparison of the C_l (T) signal for BVI; M=0.6, types A, B, C.

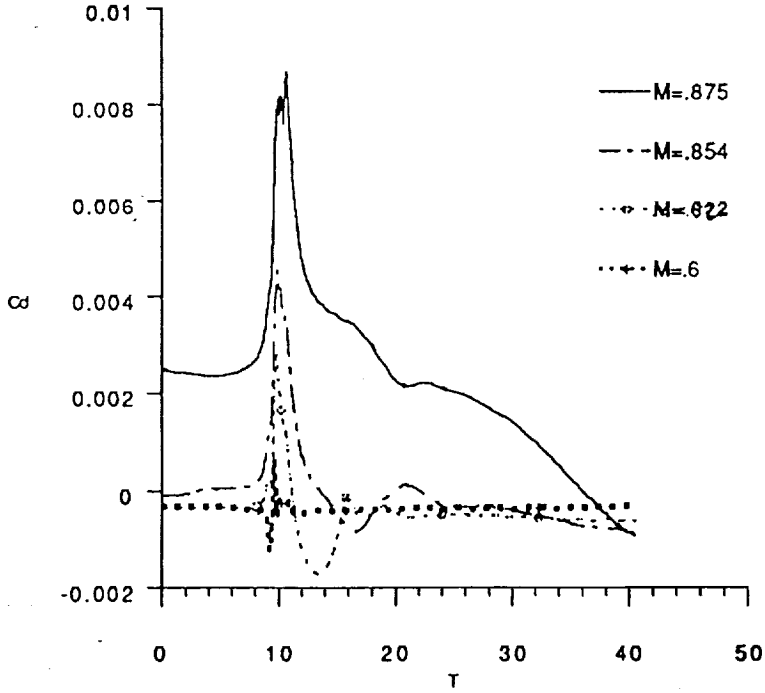

Figure 11. Comparison of the C_d (T) signal for BVI; M=0.6, types A, B, C.

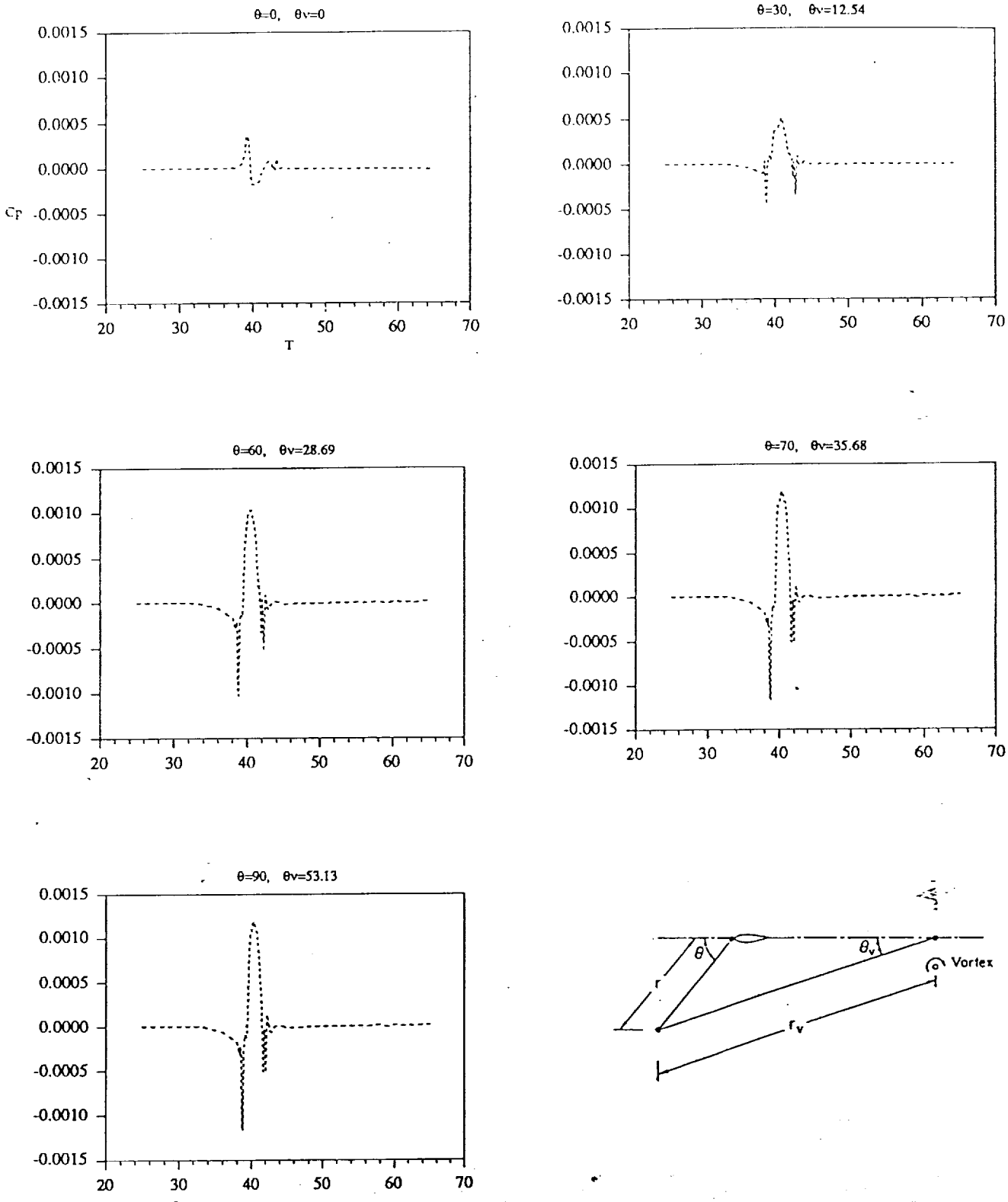

Figure 12. BVI noise directivity for M=0.6; r_v = 50 chords, span = 4 chords.

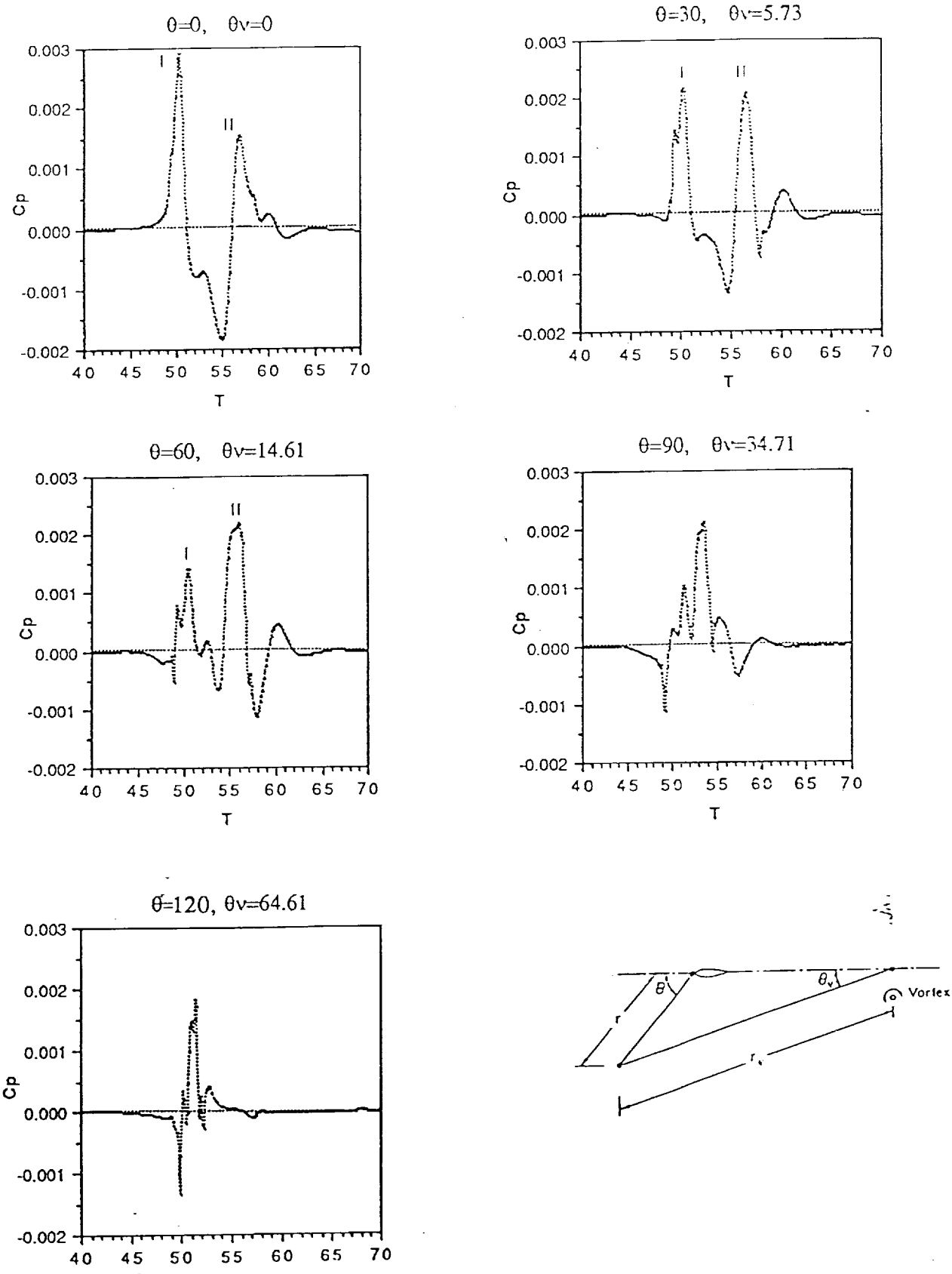

Figure 13. BVI noise directivity for type C; r_v = 50 chords, span = 4 chords, fixed observer.

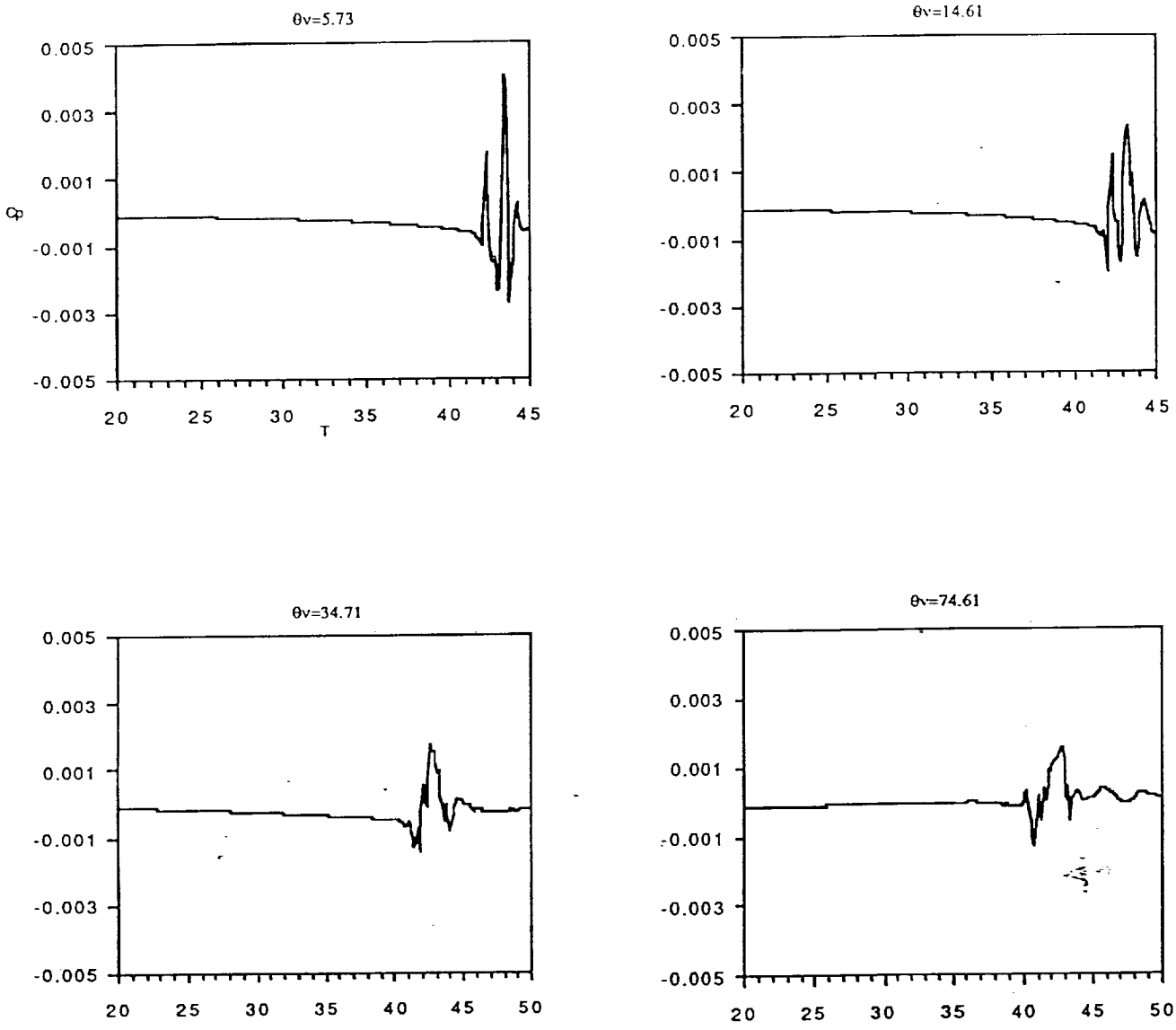

Figure 14. BVI noise directivity for type C; r_V = 50 chords, span = 4 chords, moving observer.

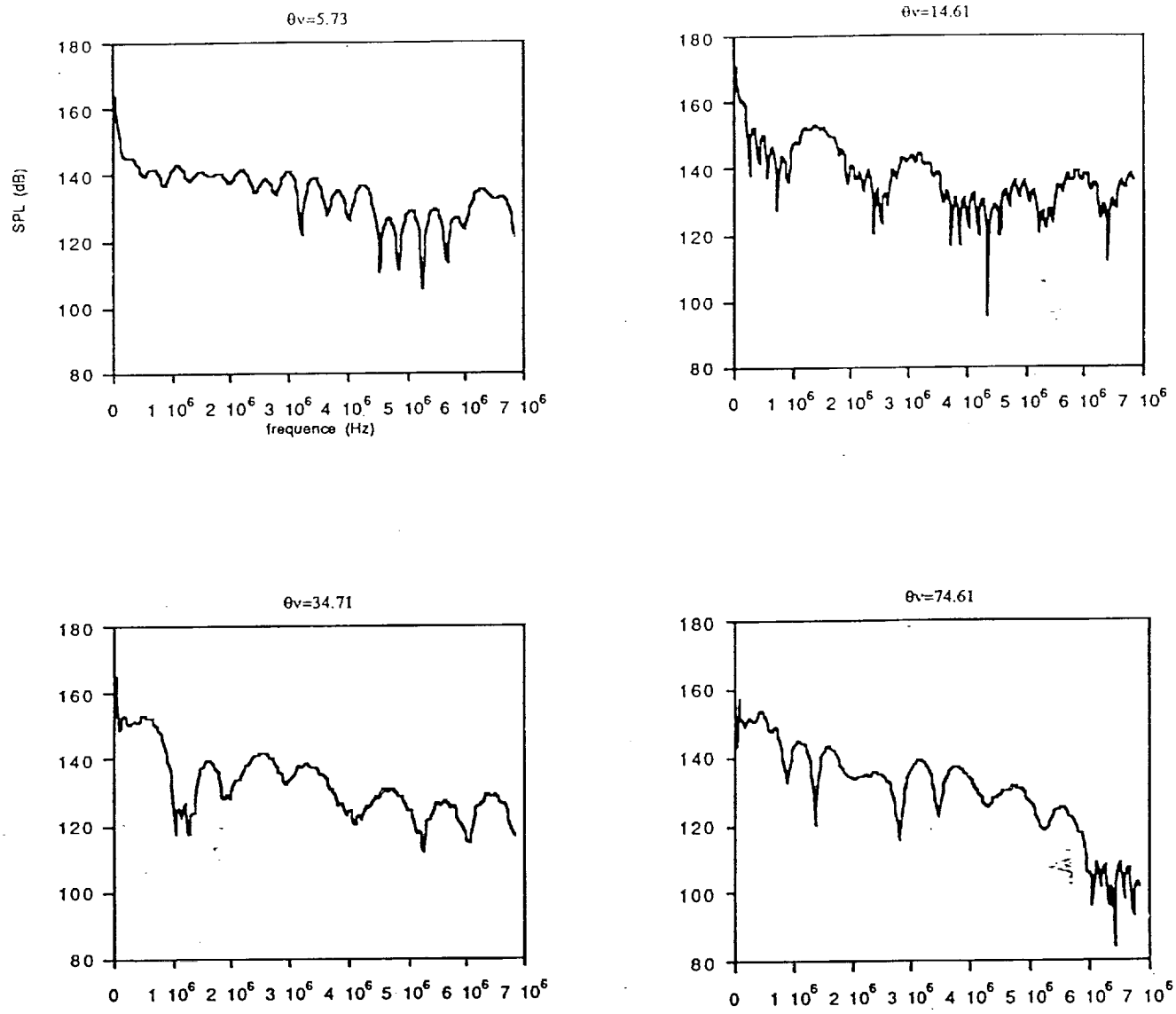

Figure 15. Noise spectra using FFT; type C, r_v = 50 chords, span = 4 chords, moving observer.

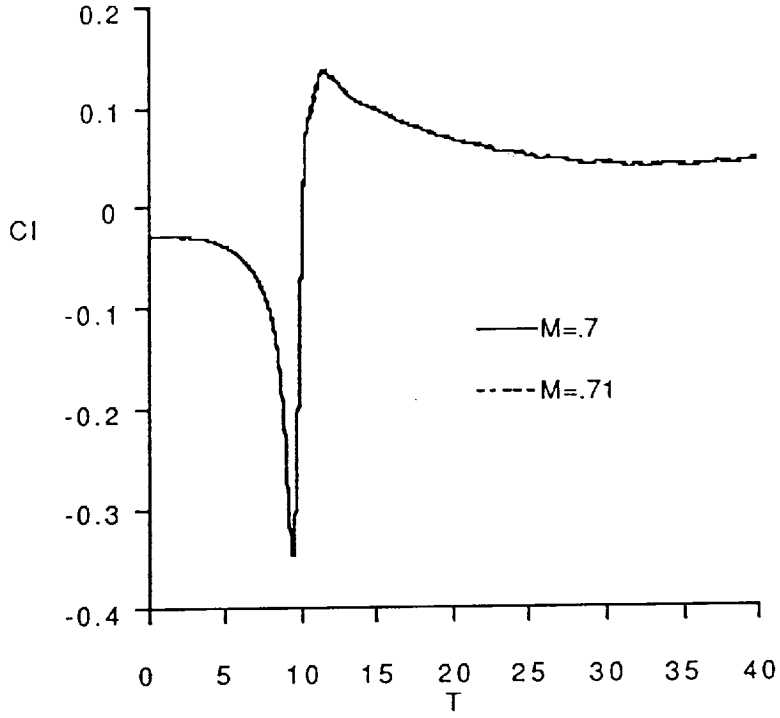

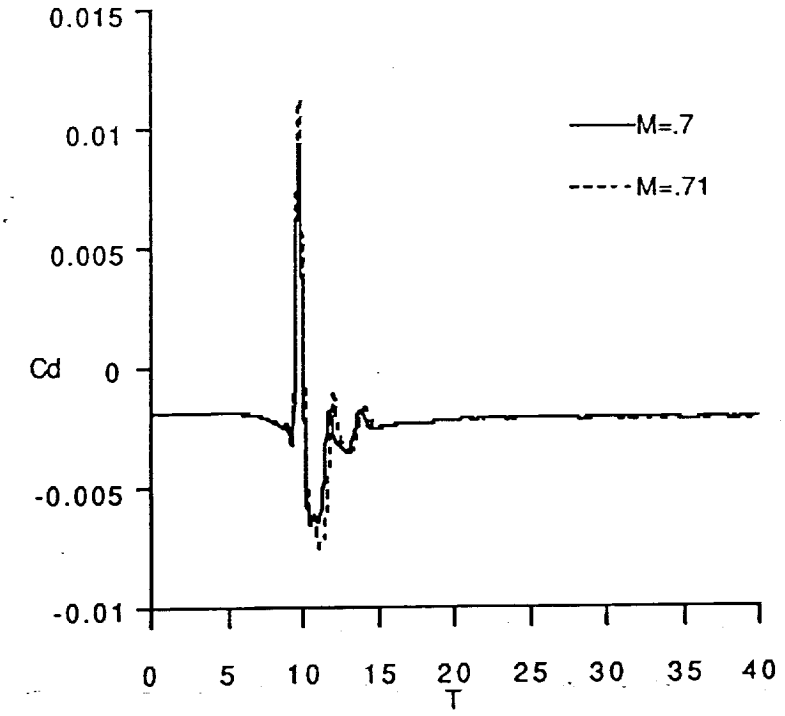

Figure 16. Cl(T) and Cd(T) signal for NACA 0012, Clv=0.65, yo=-0.26, M=0.70, 0.71

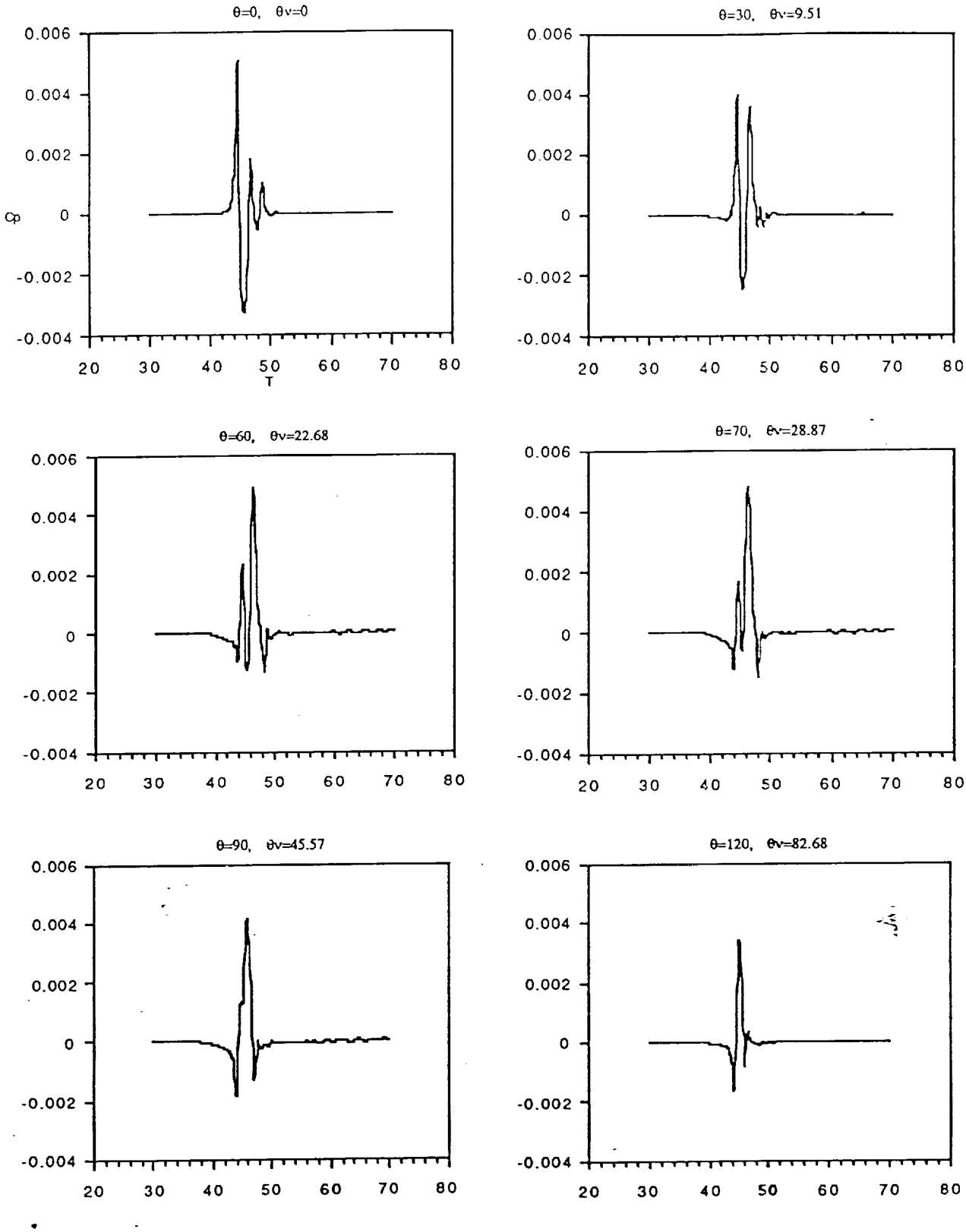

Figure 17. BVI noise directivity for NACA 0012, Clv=0.65, yo=-0.26, M=0.70, r_v = 50 chords, span = 4 chords.

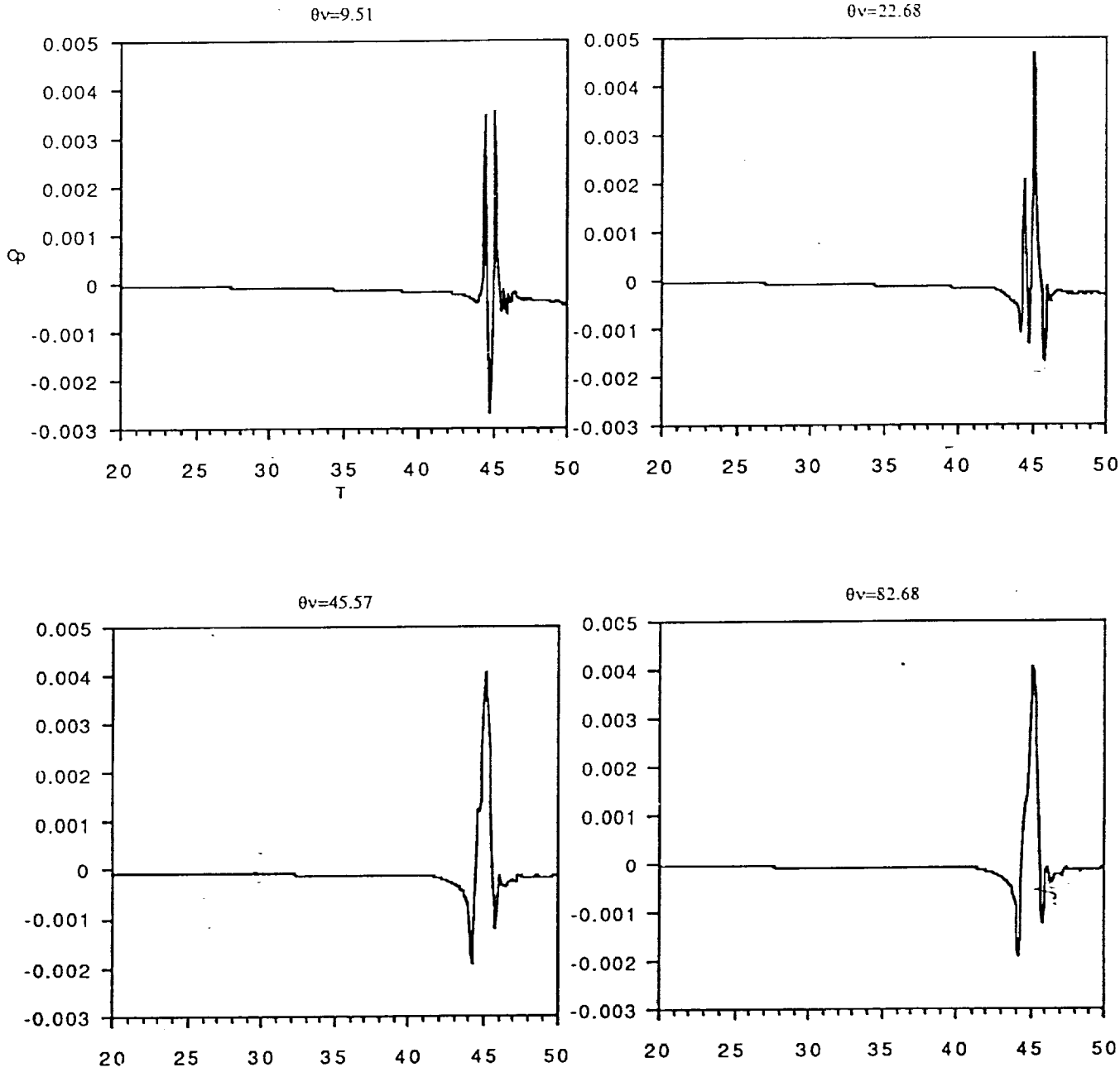

Figure 18. BVI noise directivity for NACA 0012, Clv=0.65, yo=-0.26, M=0.70, r_v = 50 chords, span = 4 chords, moving observer.

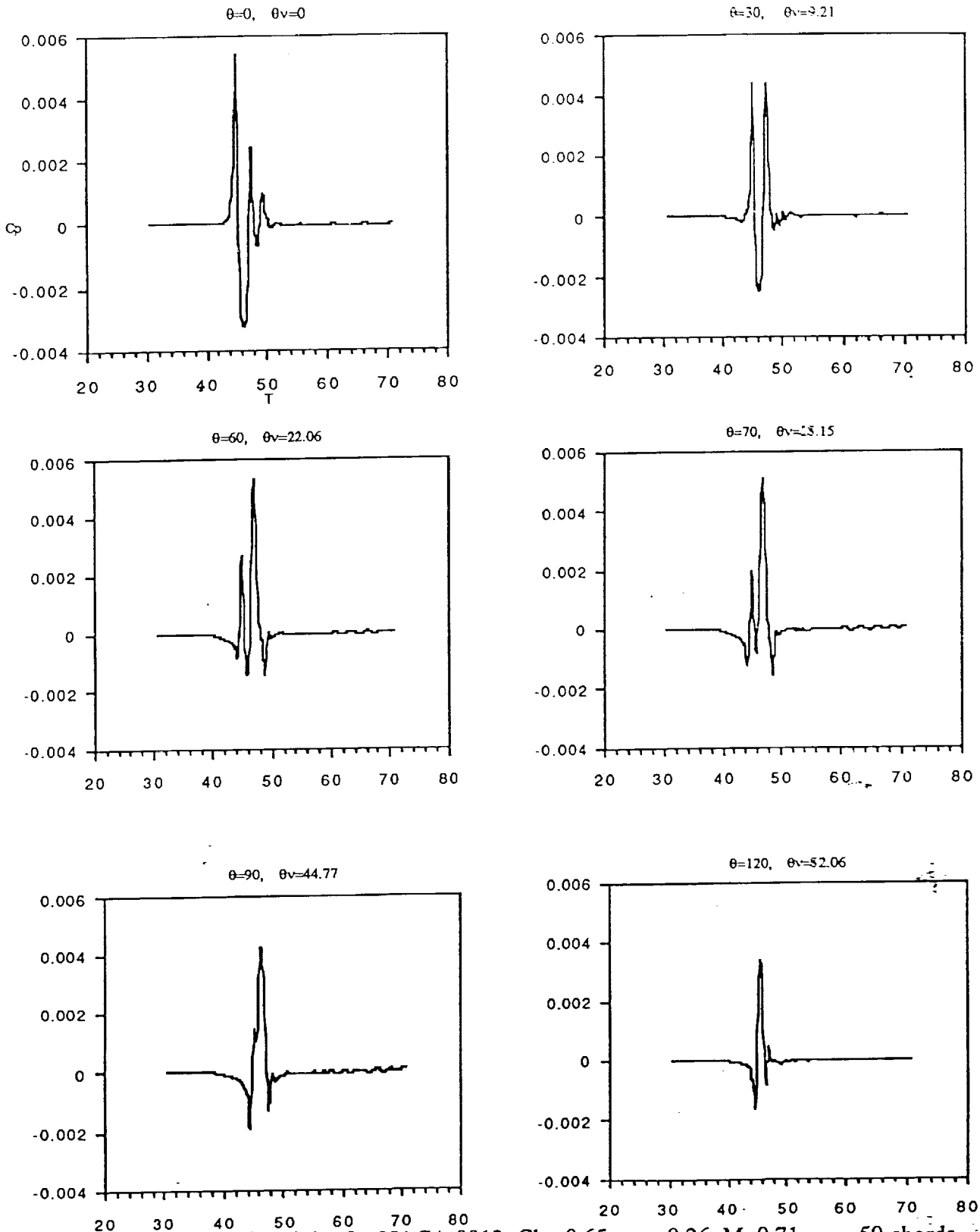

Figure 19. BVI noise directivity for NACA 0012, Clv=0.65, yo=-0.26, M=0.71, r_v = 50 chords, span = 4 chords.

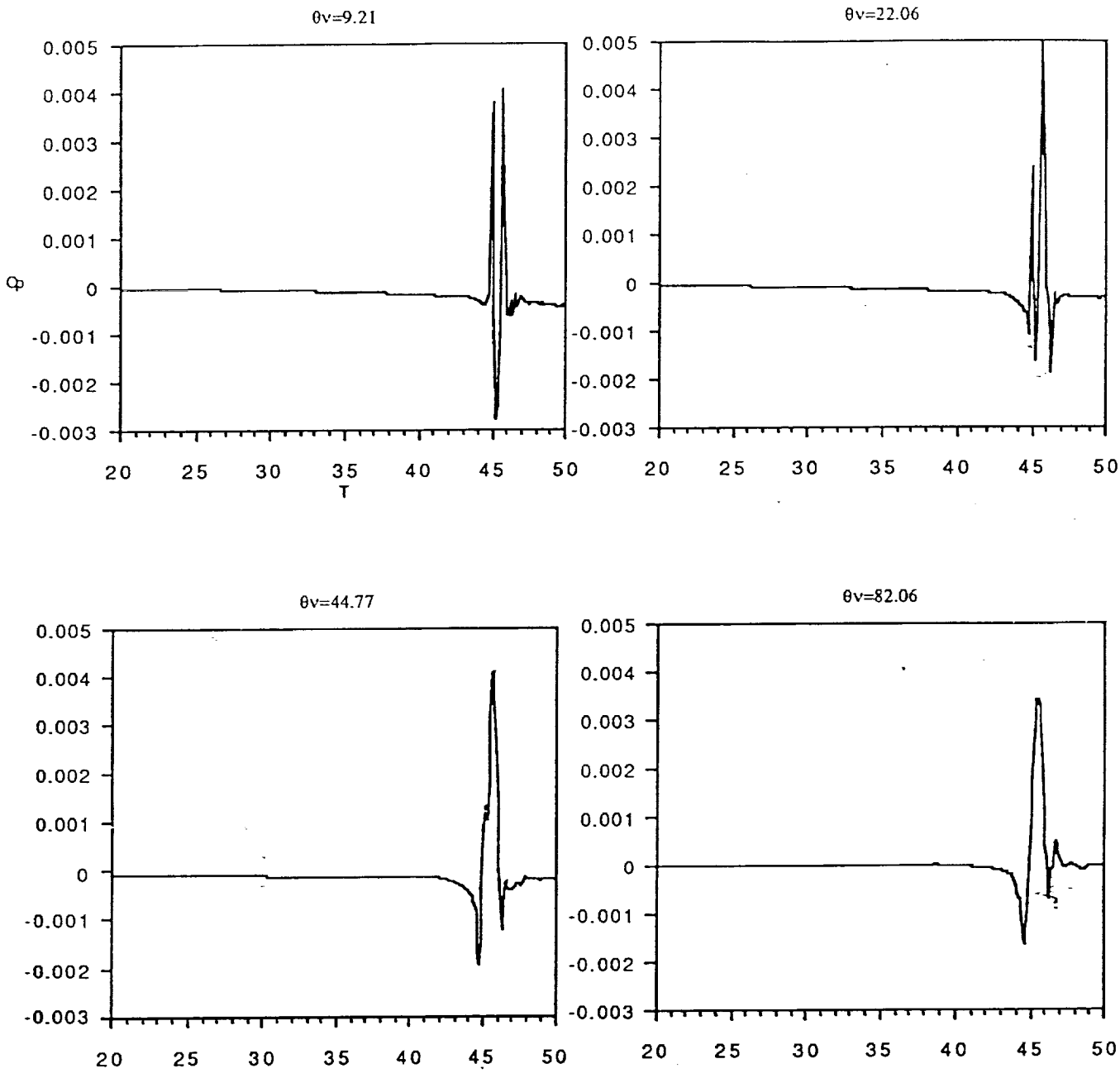

Figure 20. BVI noise directivity for NACA 0012, Clv=0.65, yo=-0.26, M=0.71, r_v = 50 chords, span = 4 chords, moving observer.

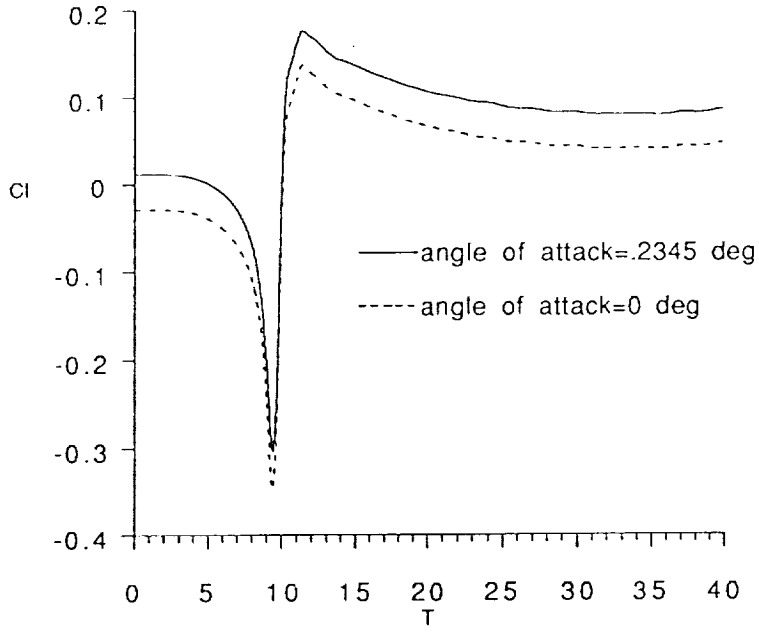

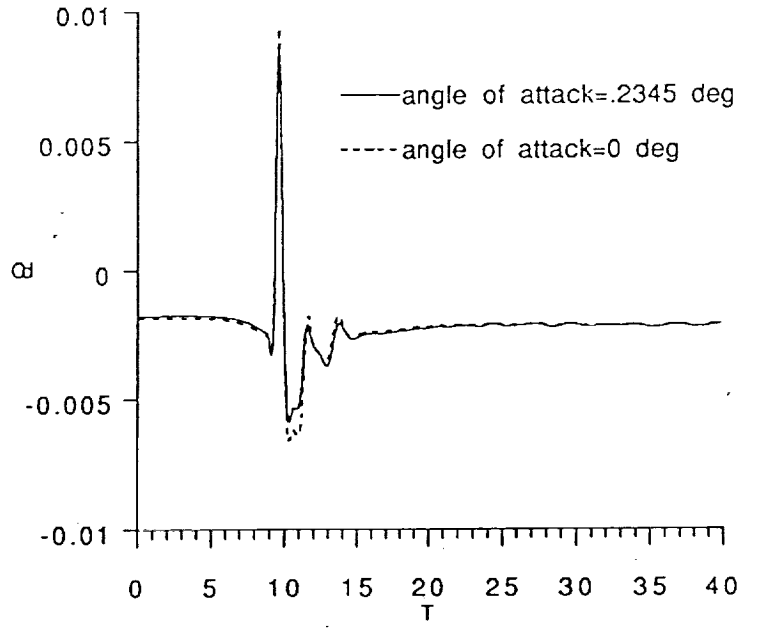

Figure 21. Cl(T) and Cd(T) signal for NACA 0012, Clv=0.65, yo=-0.26, M=0.70, Cl (without vortex)= 0.04, 0.0.

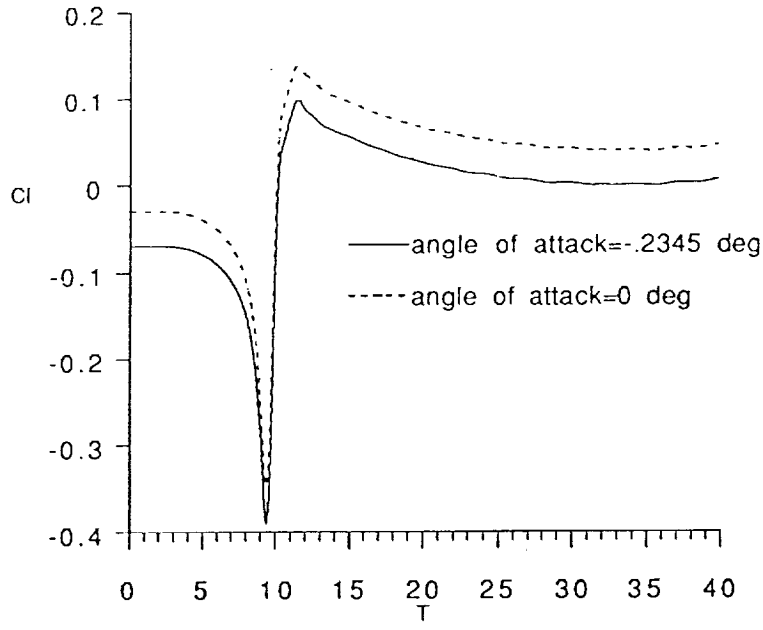

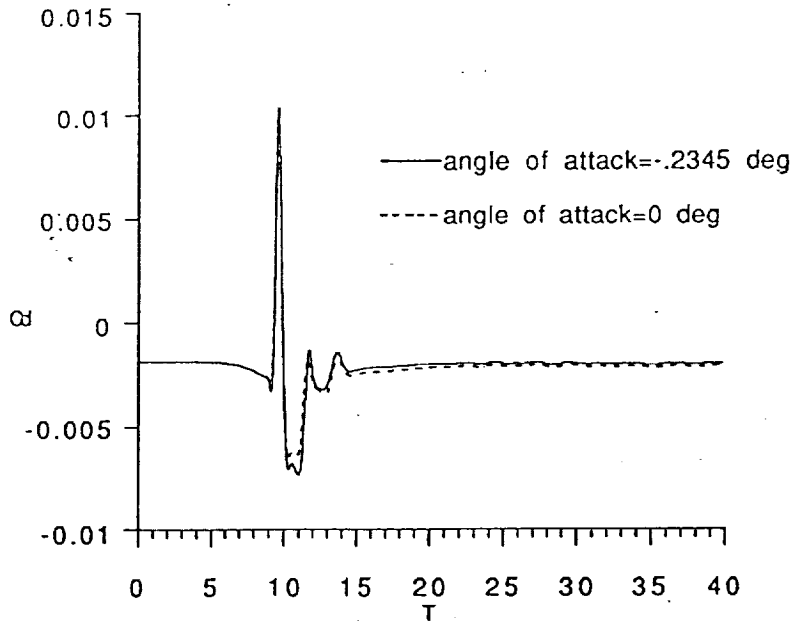

Figure 22. Cl(T) and Cd(T) signal for NACA 0012, Clv=0.65, yo=-0.26, M=0.70, Cl (without vortex)= -0.04, 0.0.

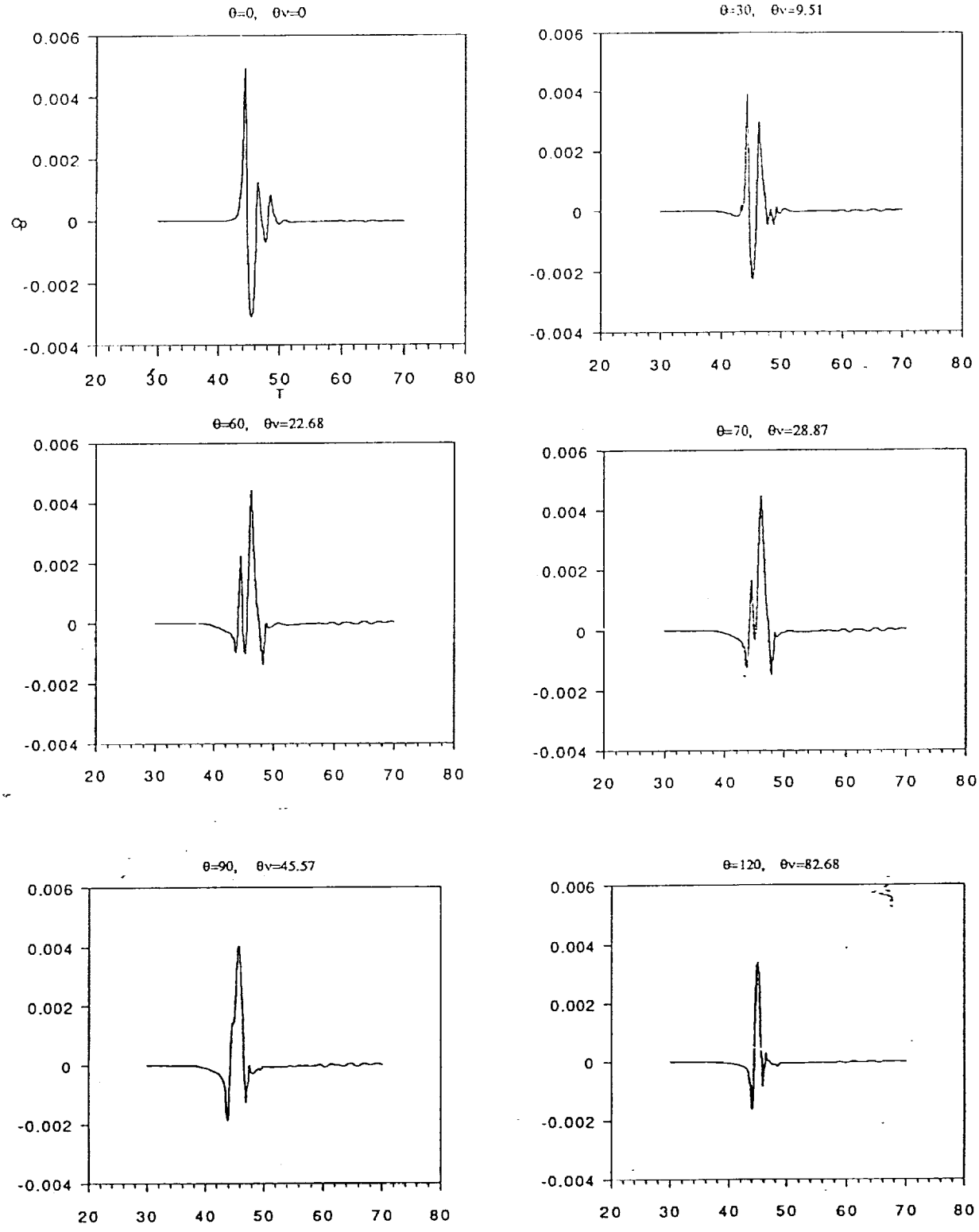

Figure 23. BVI noise directivity for NACA 0012, Clv=0.65, yo=-0.26, M=0.70, Cl (without vortex)= 0.04, r_v = 50 chords, span = 4 chords.

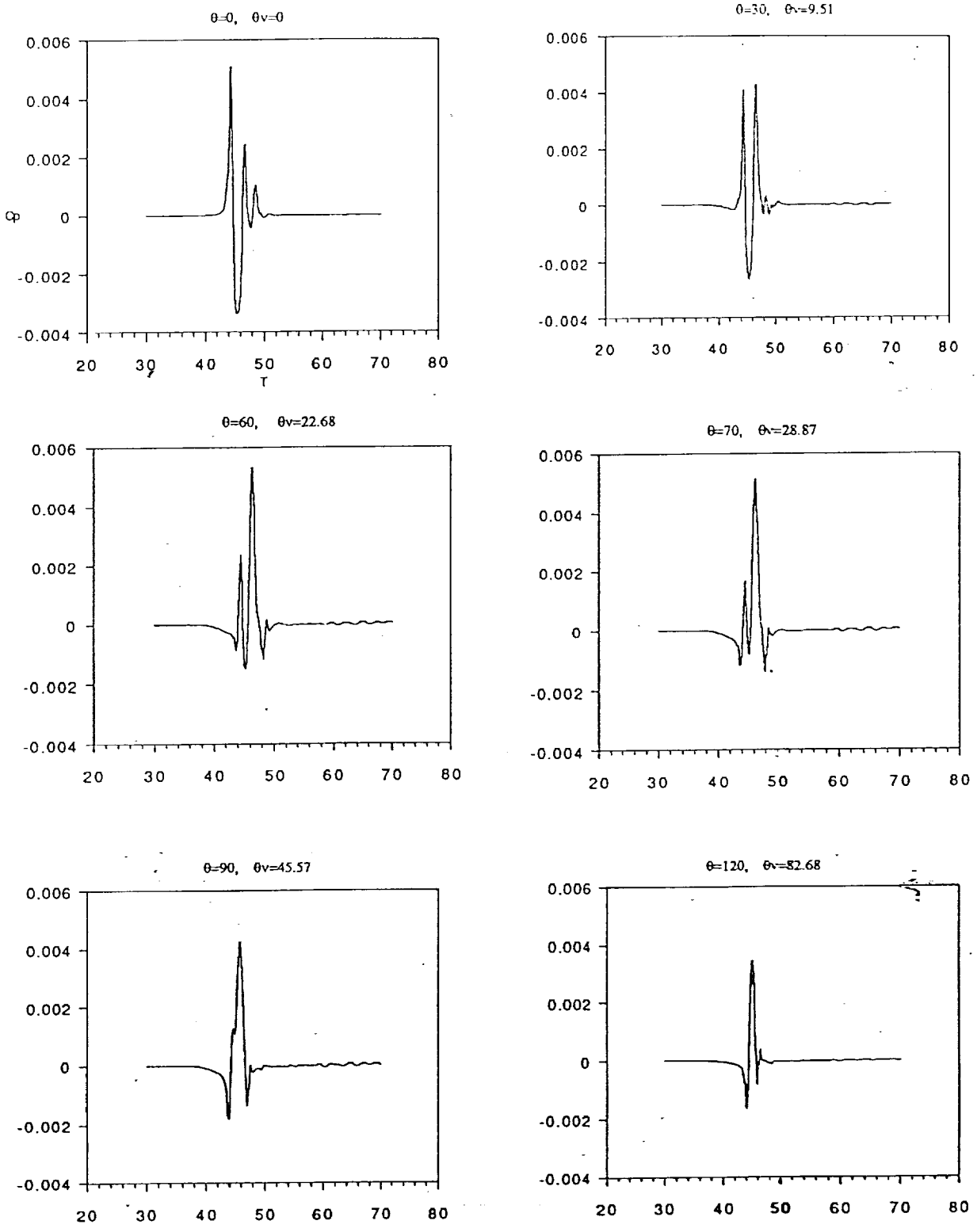

Figure 24. BVI noise directivity for NACA 0012, Clv=0.65, yo=-0.26, M=0.70, Cl (without vortex)= -0.04, r_v = 50 chords, span = 4 chords.

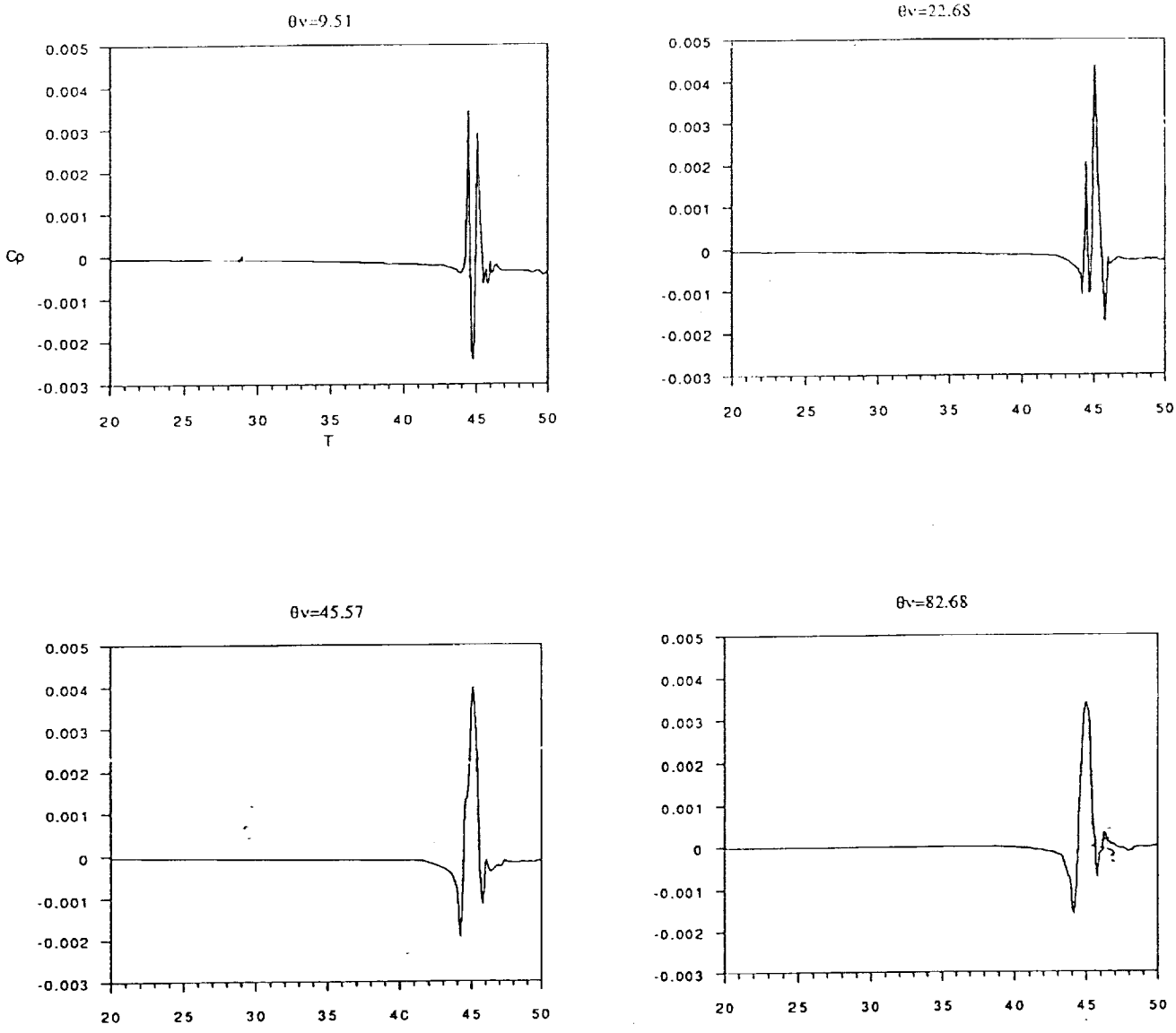

Figure 25. BVI noise directivity for NACA 0012, Clv=0.65, yo=-0.26, M=0.70, Cl (without vortex)= 0.04, r_v = 50 chords, span = 4 chords, moving observer.

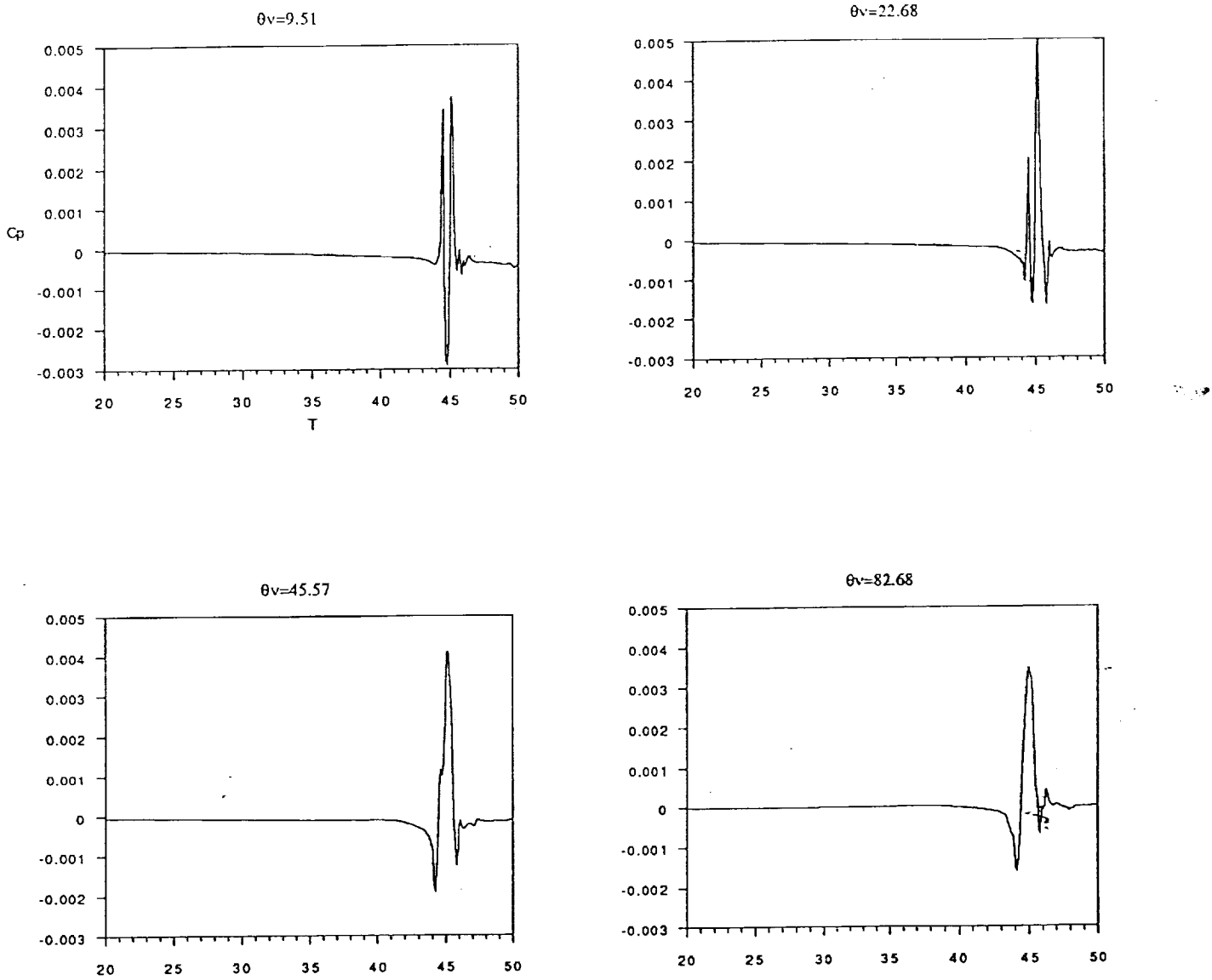

Figure 26. BVI noise directivity for NACA 0012, Clv=0.65, yo=-0.26, M=0.70, Cl (without vortex)= -0.04, r_v = 50 chords, span = 4 chords, moving observer.

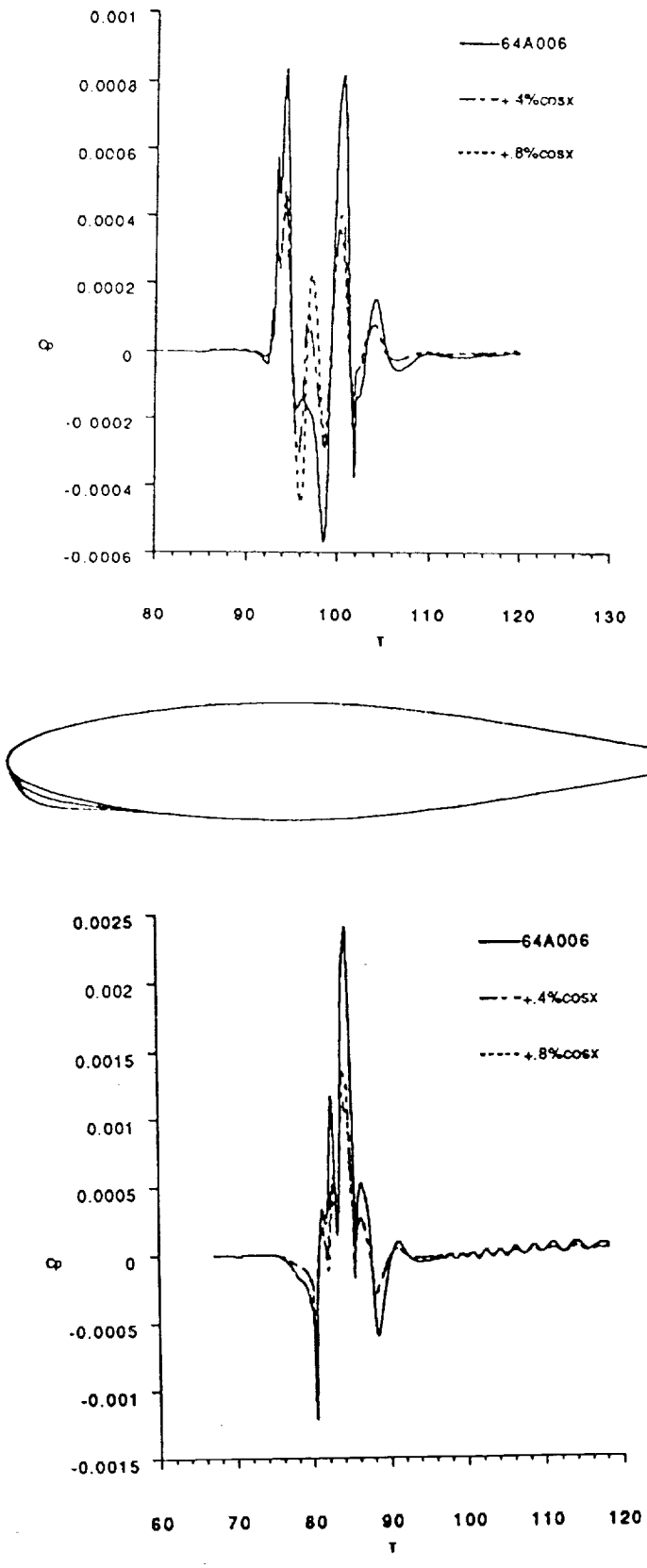

Figure 27. Cosine curve modification of 64A006 and far-field BVI noise (r_V=50, θ=30°, 90°); thickness: 0.4%, 0.8%, modification interval: 38%.

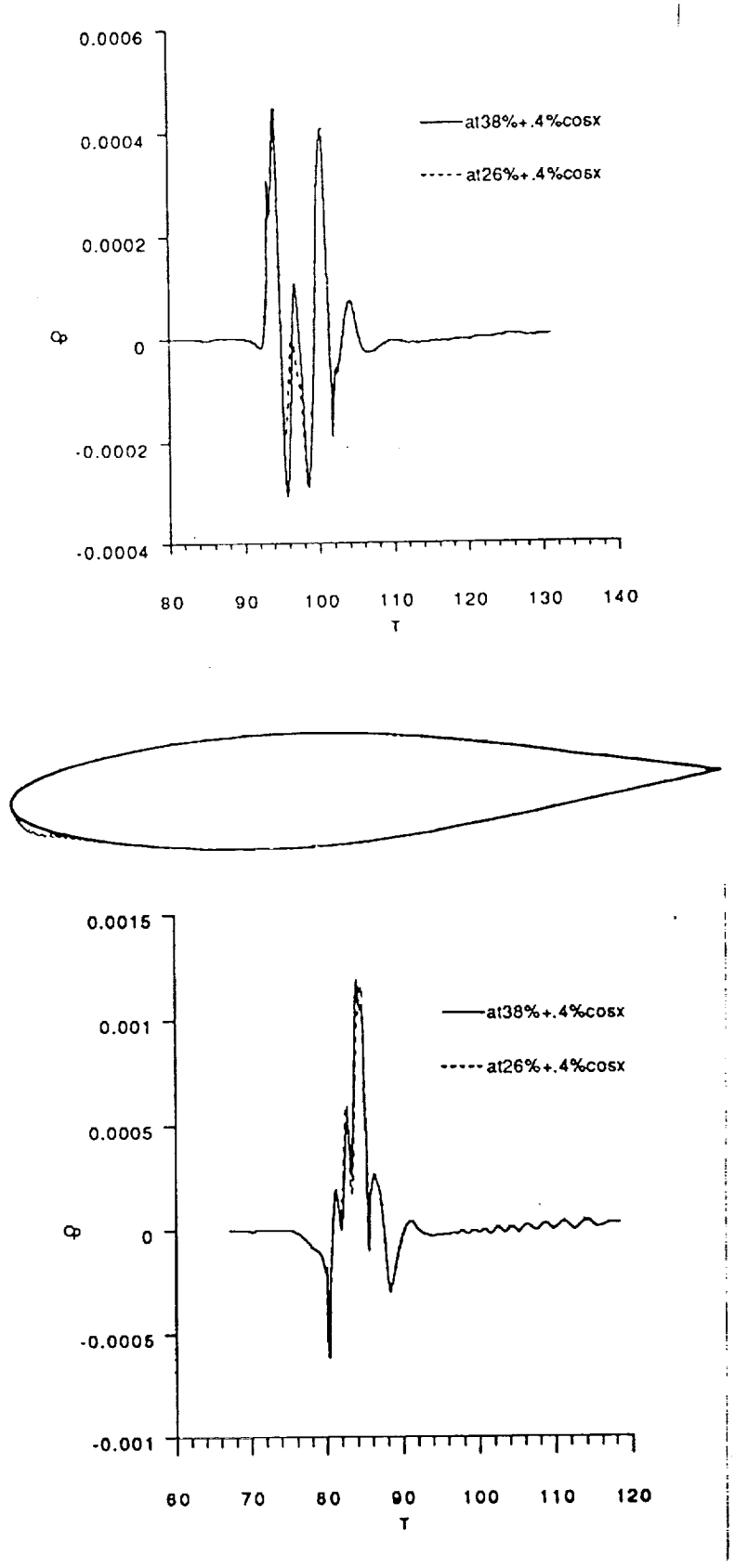

Figure 28. Cosine curve modification of 64A006 and far-field BVI noise (r_V=50, θ=30°, 90°); thickness: 0.4%, modification intervals: 26%, 38%.

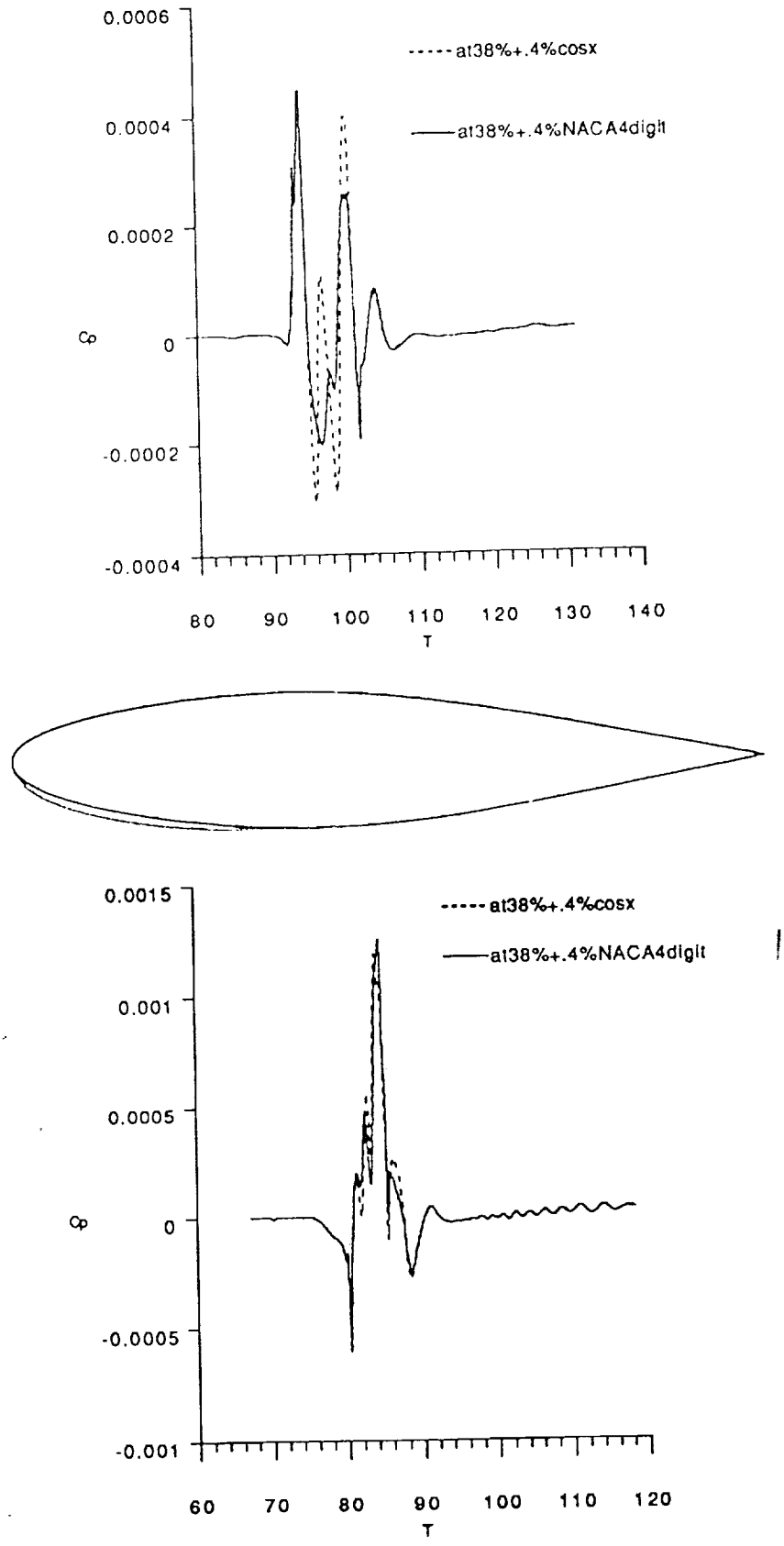

Figure 29. Cosine and NACA 4-digit thickness curve modification of 64A006 and far-field BVI noise (r_V=50, θ=30°, 90°); thickness: 0.4%, modification interval: 38%.

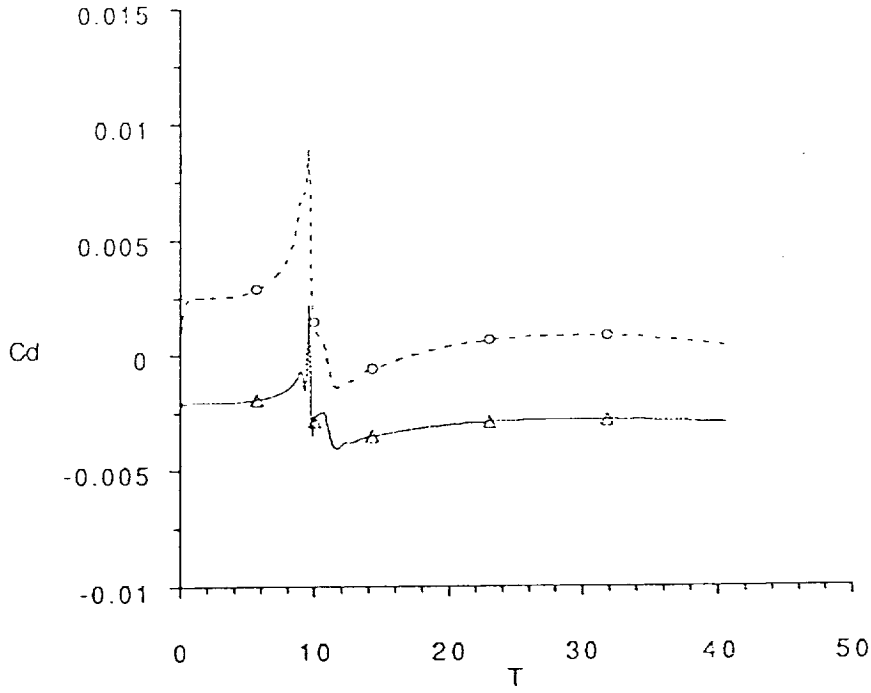

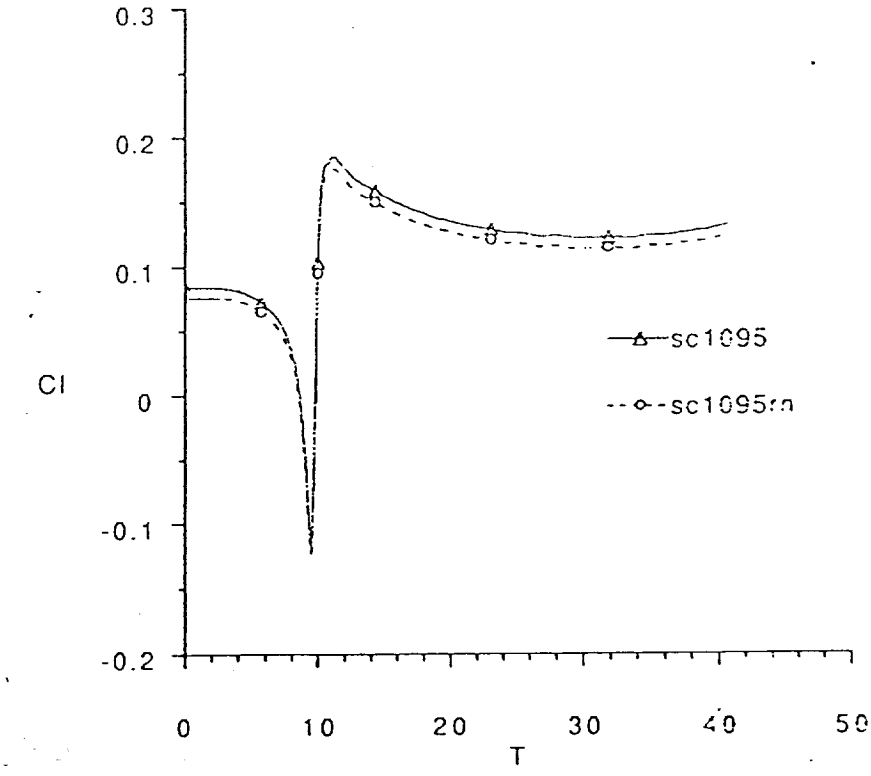

Figure 30. Cd(T) and Cl(T) for SC1095 and SC1095rn at M_{∞}=0.6.

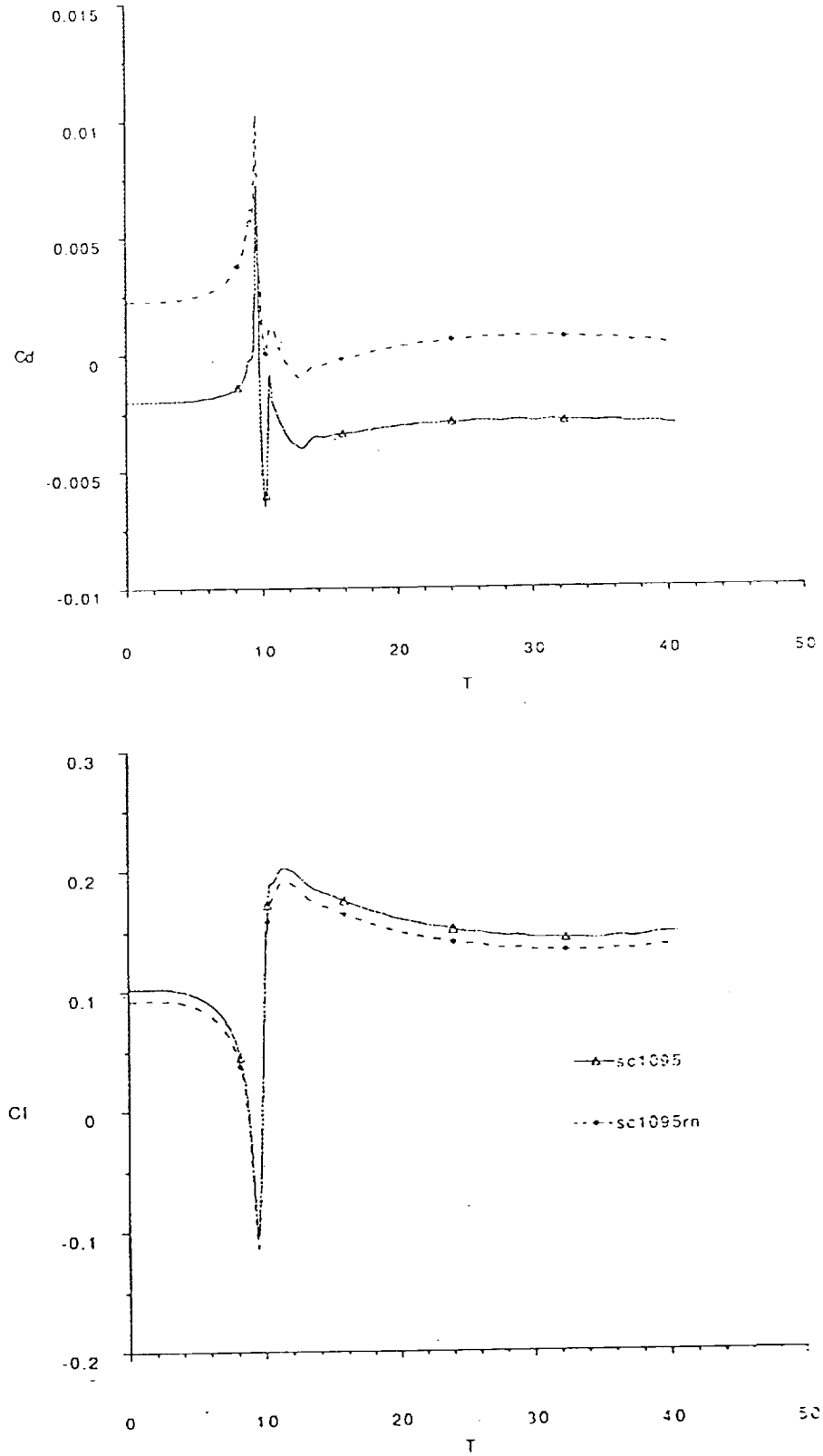

Figure 31. Cd(T) and Cl(T) for SC1095 and SC1095rn at M_∞=0.7.

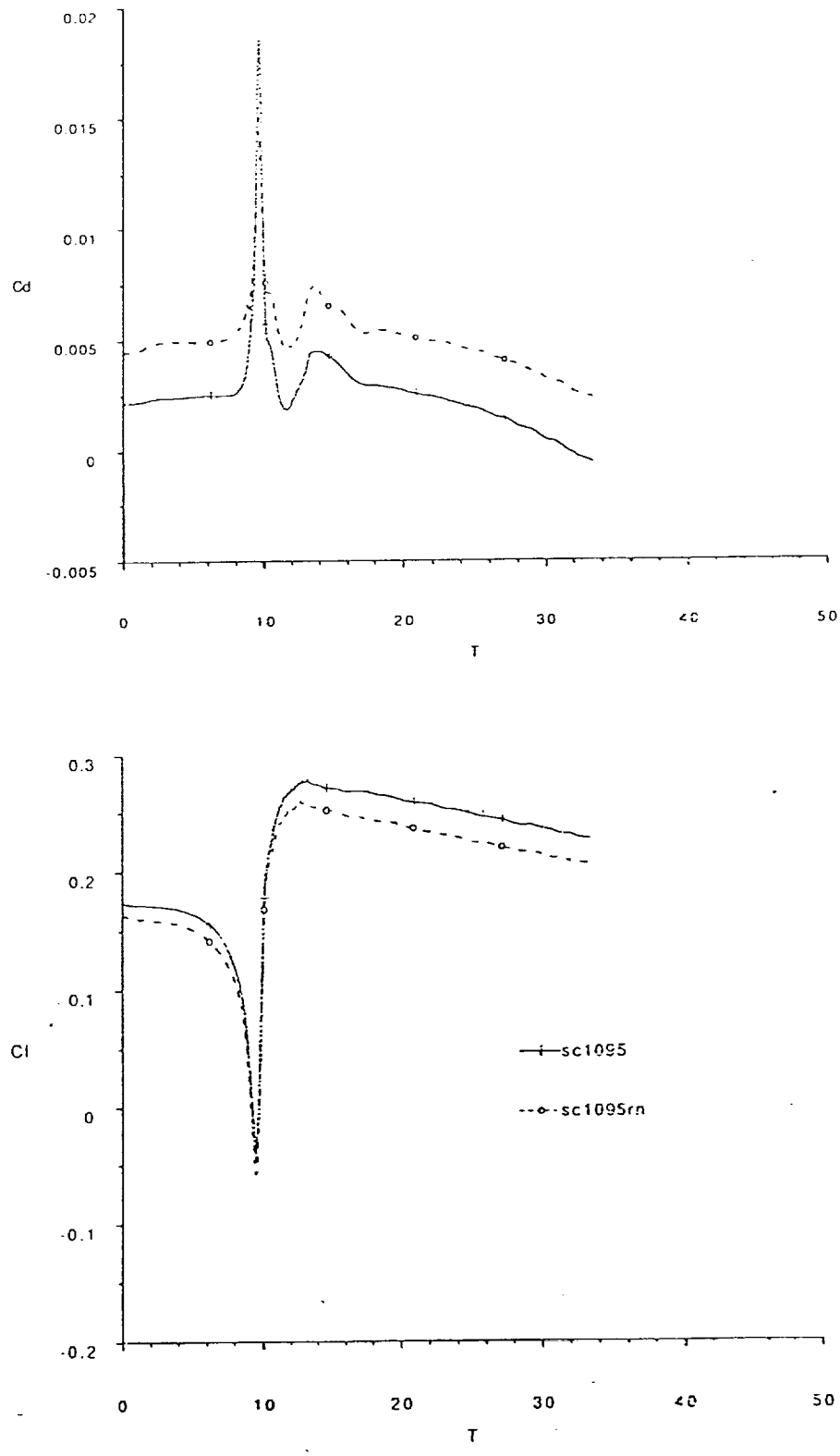

Figure 32. Cd(T) and Cl(T) for SC1095 and SC1095rn at M_{∞}=0.8.

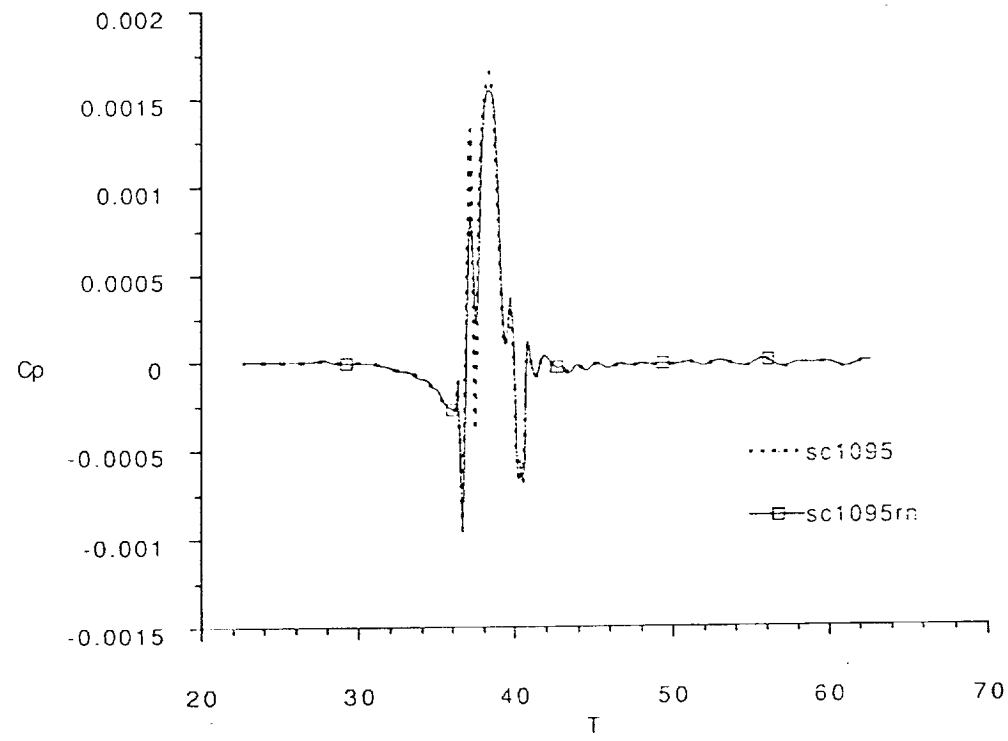

Figure 33. BVI noise Cp(T) signal for SC1095 and SC1095rn at M_∞=0.6
(r=20 chords, θ=30°, span=8 chords)

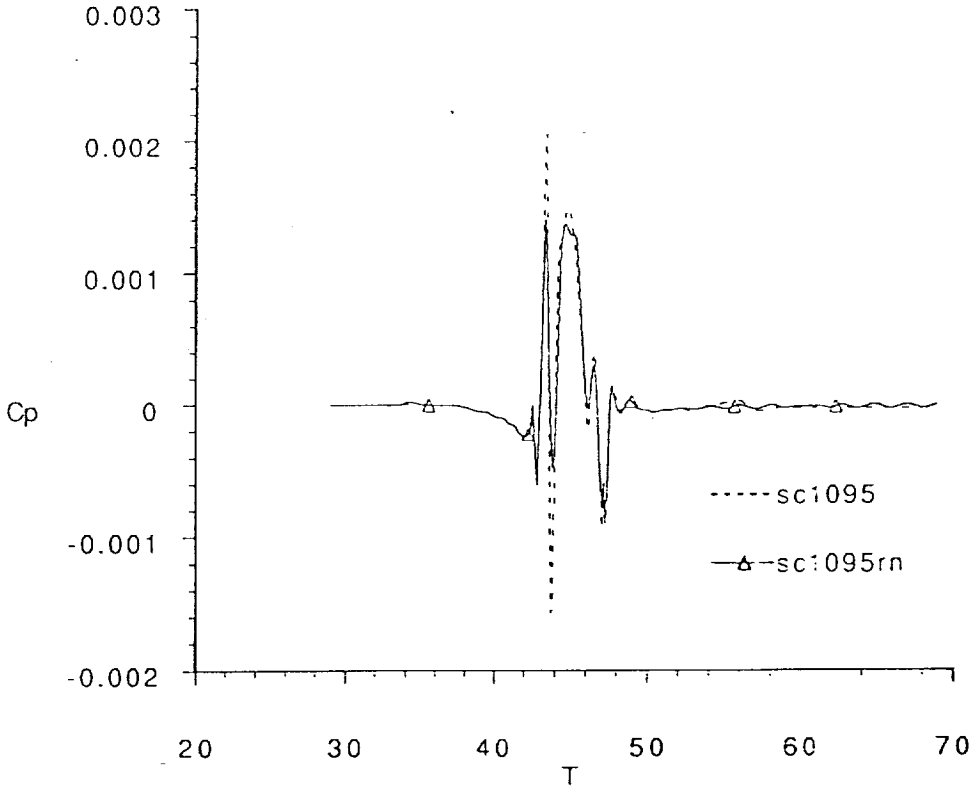

Figure 34. BVI noise Cp(T) signal for SC1095 and SC1095rn at M_∞=0.65
(r=20 chords, θ=30°, span=8 chords)

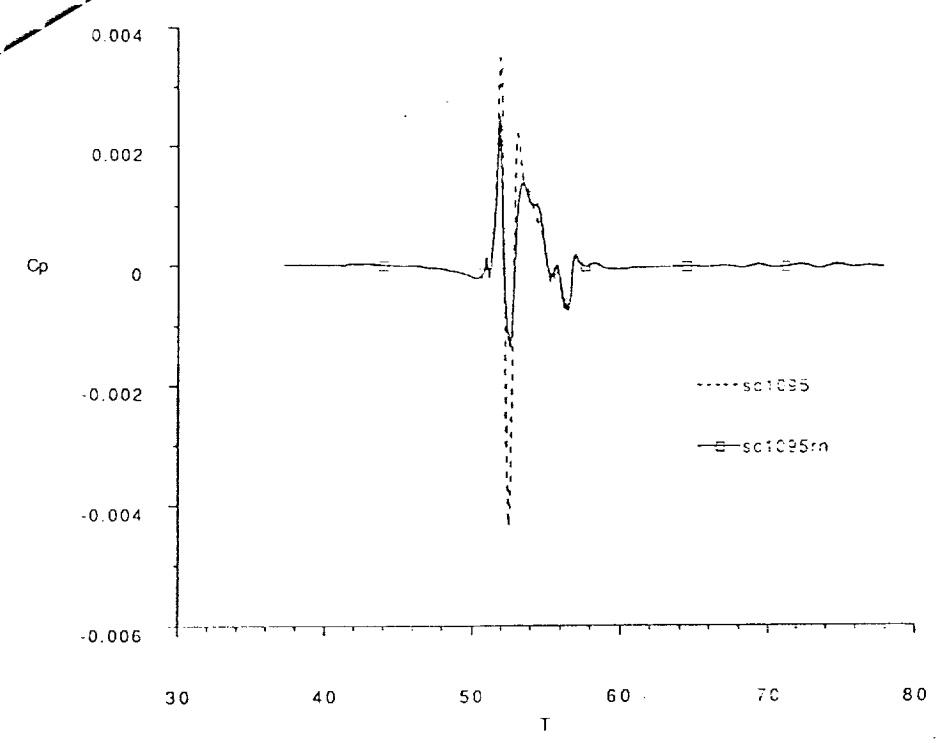

Figure 35. BVI noise Cp(T) signal for SC1095 and SC1095rn at M_∞=0.7
(r=20 chords, θ=30°, span=8 chords)

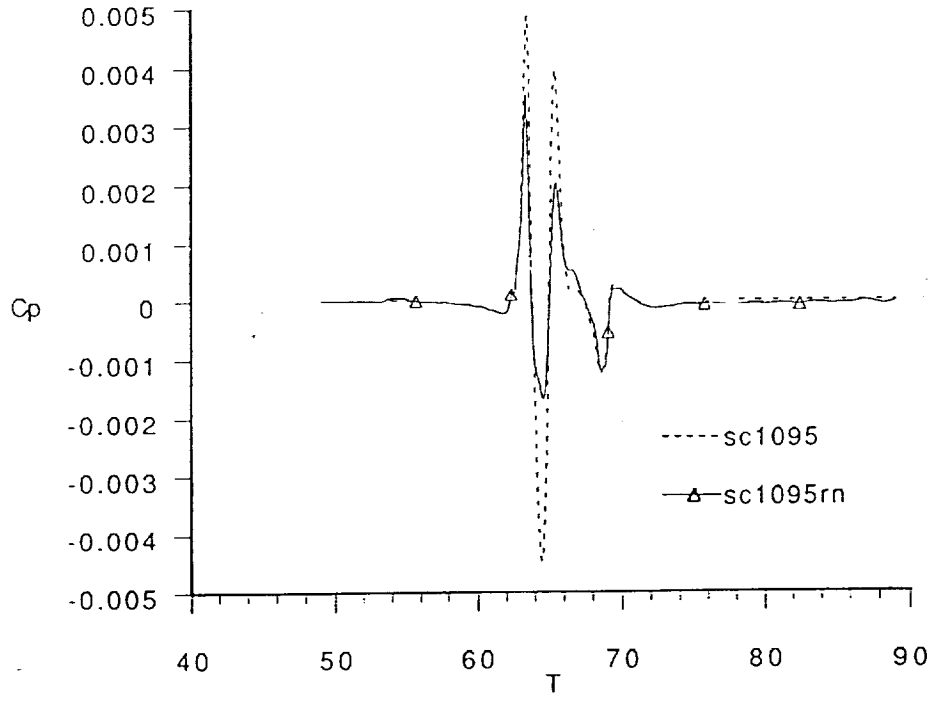

Figure 36. BVI noise Cp(T) signal for SC1095 and SC1095rn at M_∞=0.75
(r=20 chords, θ=30°, span=8 chords)

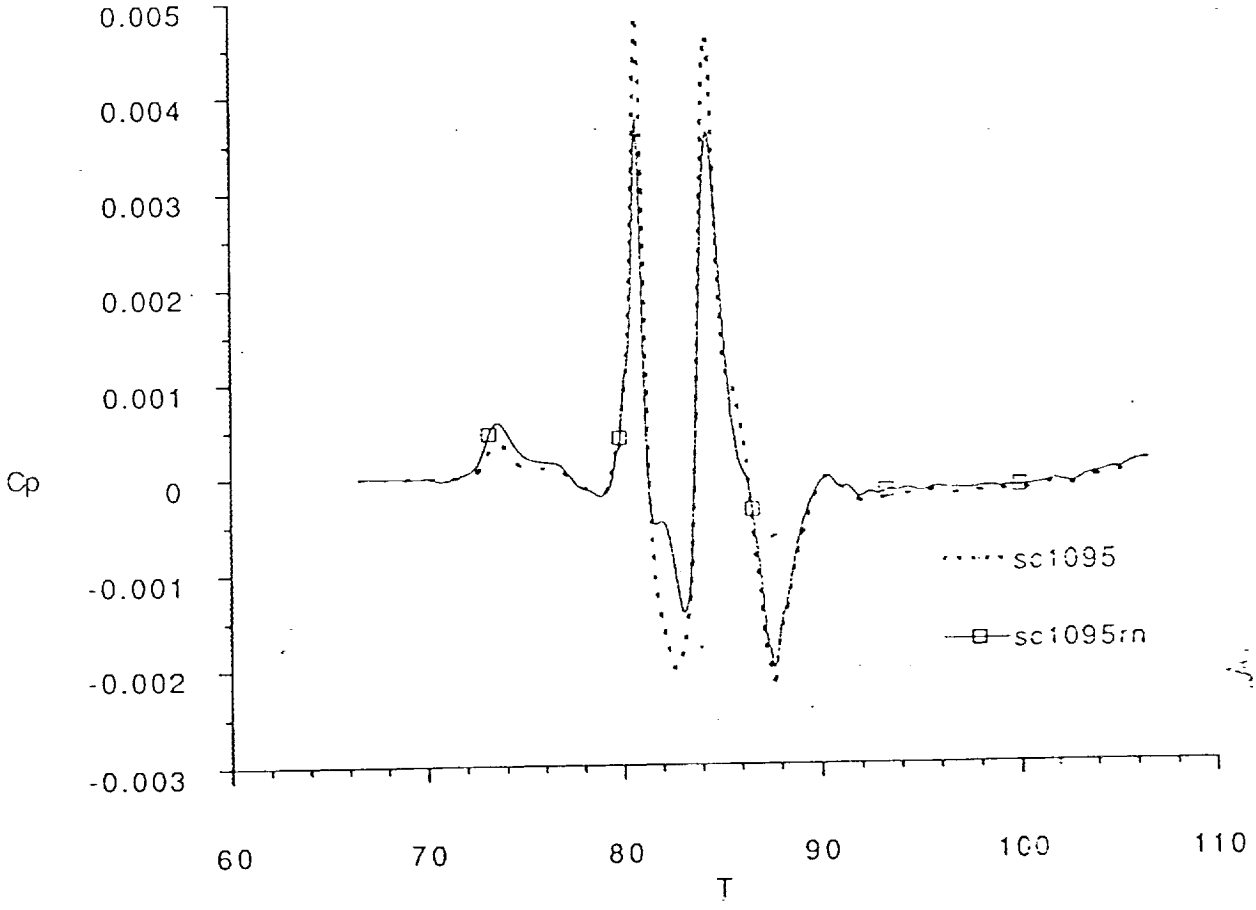

Figure 37. BVI noise Cp(T) signal for SC1095 and SC1095rn at M_∞=0.8
(r=20 chords, θ=30°, span=8 chords)

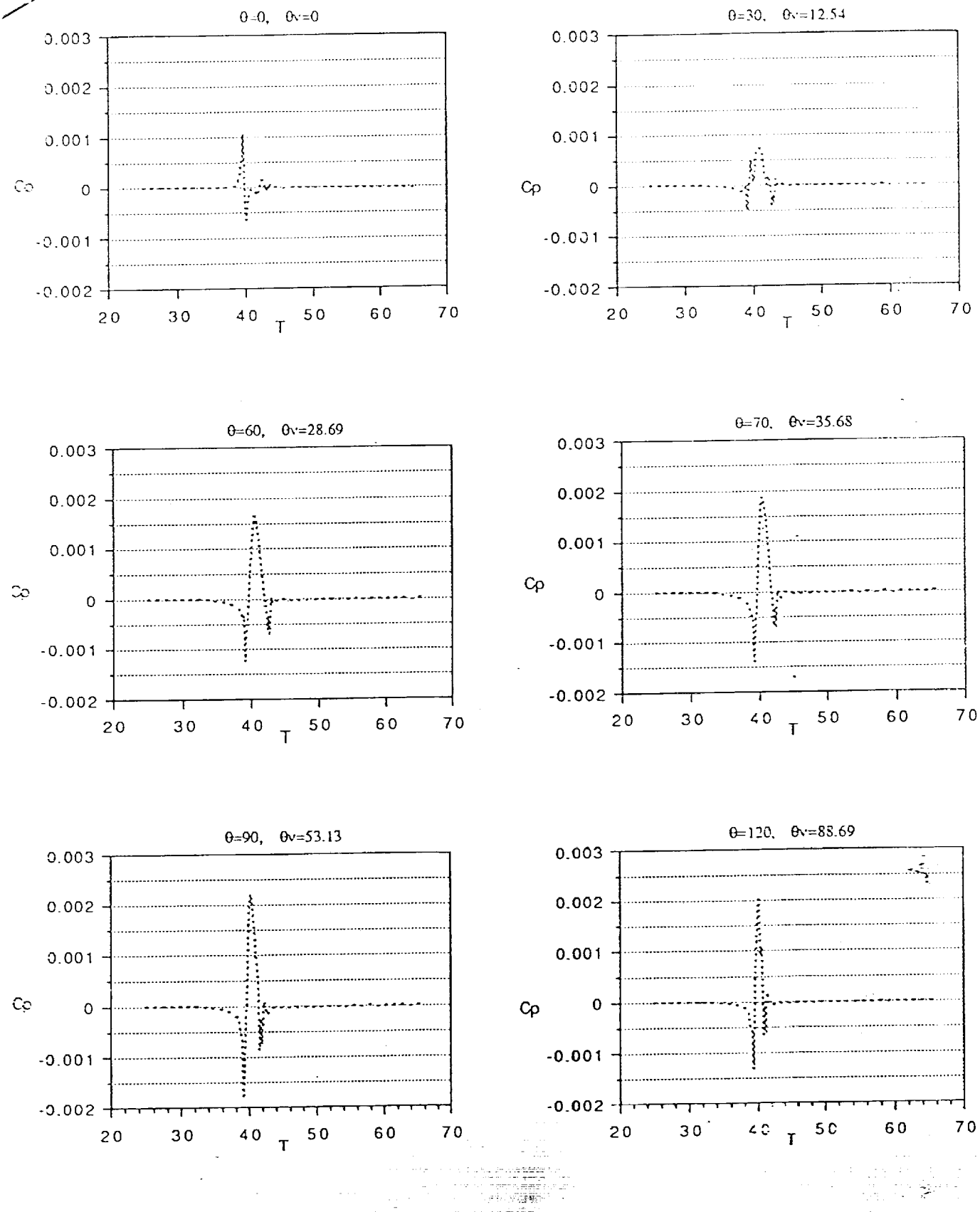

Figure 38. BVI noise directivity for airfoil SC1095 at M_∞=0.6; r_v=50 chords, span=4 chords

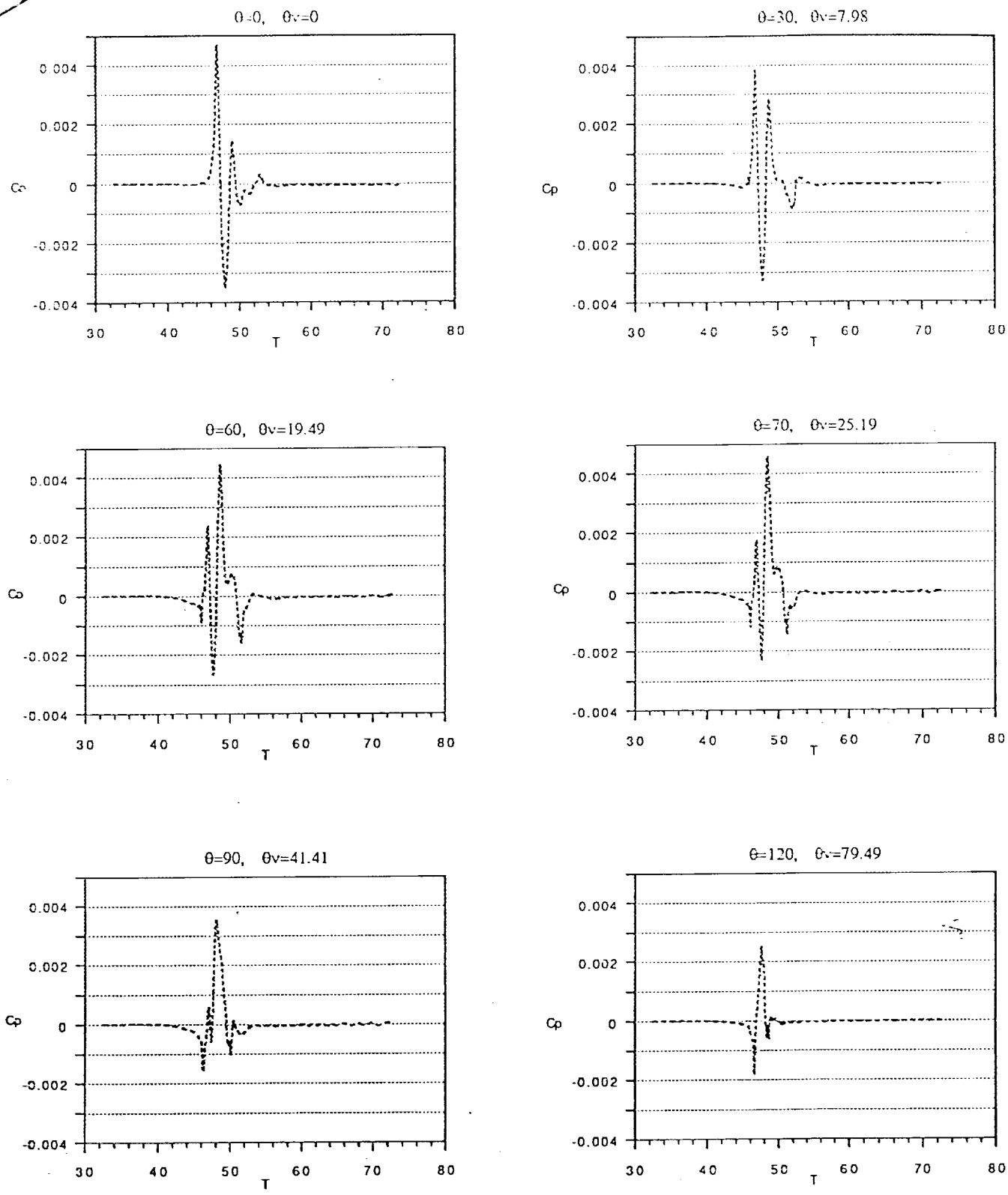

Figure 39. BVI noise directivity for airfoil SC1095 at M_∞=0.7; r_v=50 chords, span=4 chords

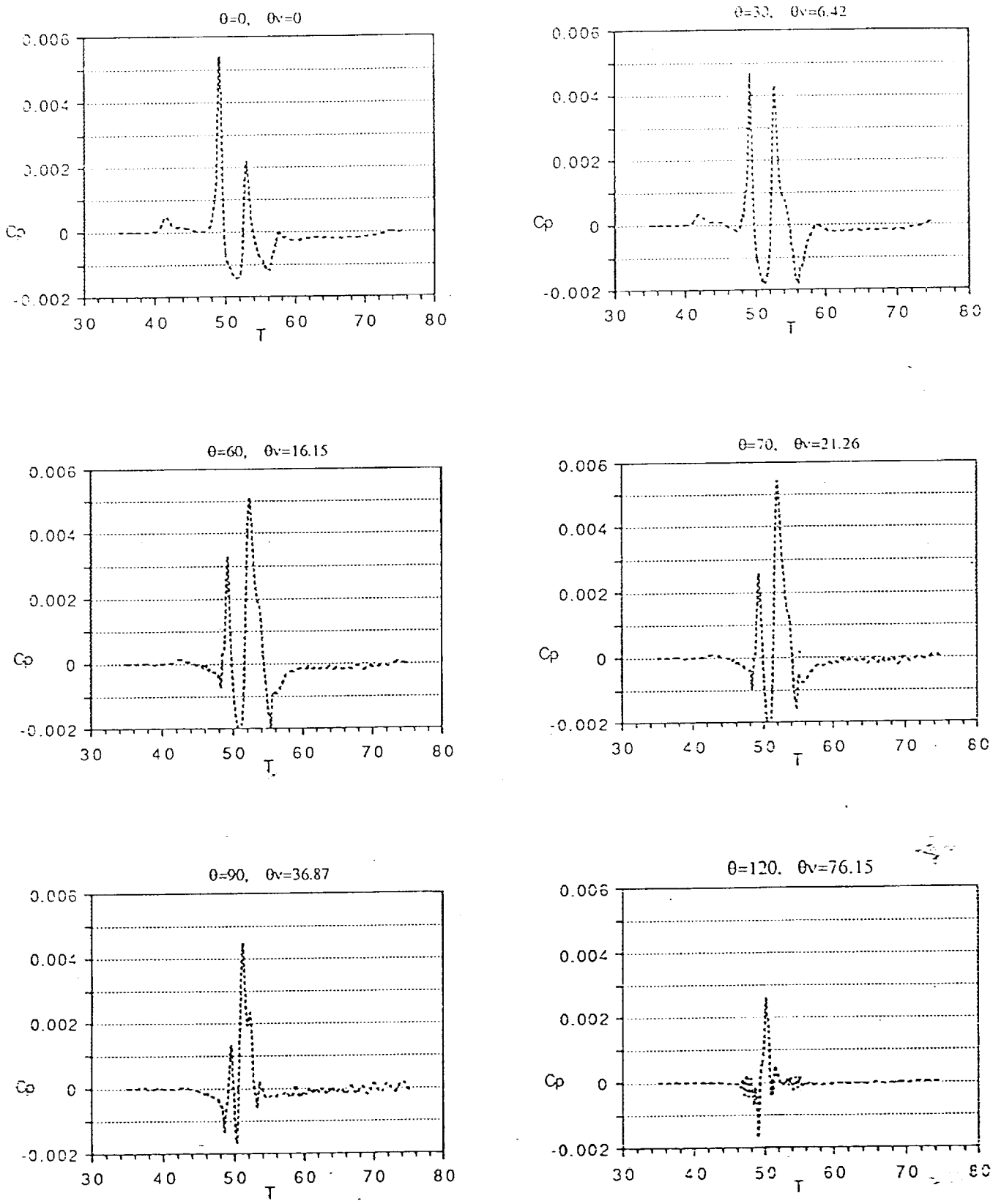

Figure 40. BVI noise directivity for airfoil SC1095 at M_∞=0.8; r_v=50 chords, span=4 chords

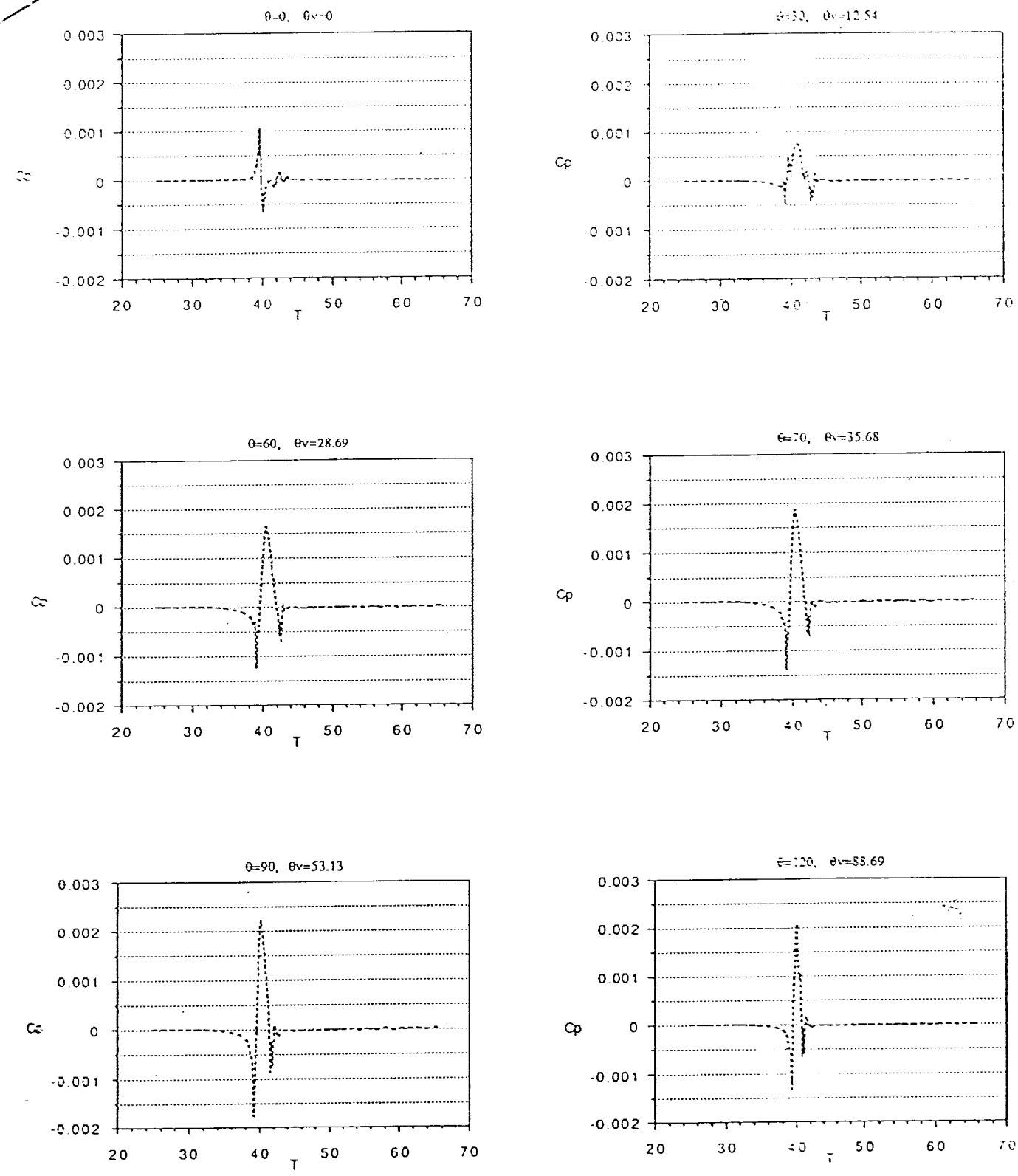

Figure 41. BVI noise directivity for airfoil SC1095rn at M_∞=0.6; r_v=50 chords, span=4 chords

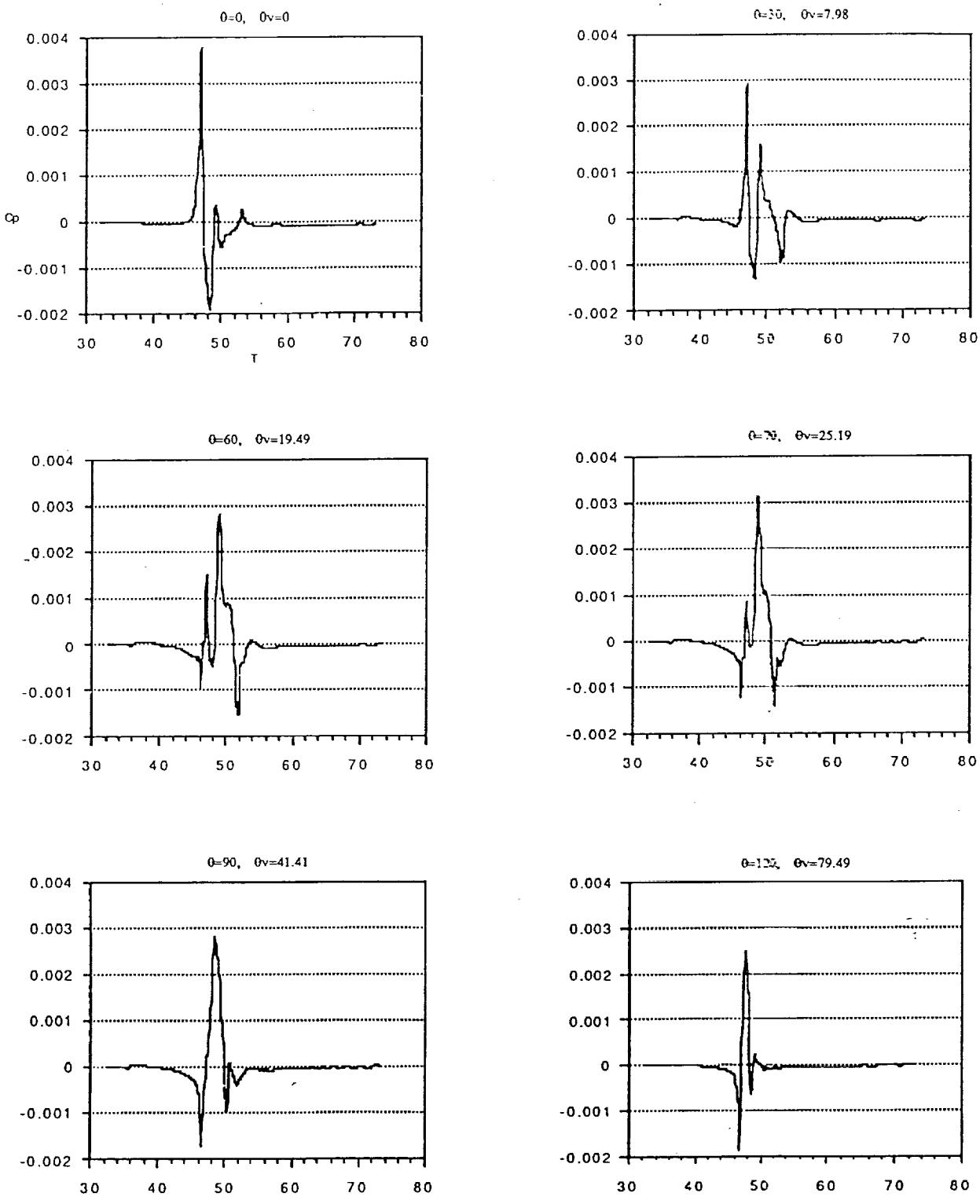

Figure 42. BVI noise directivity for airfoil SC1095rn at M_∞=0.7; r_v=50 chords, span=4 chords

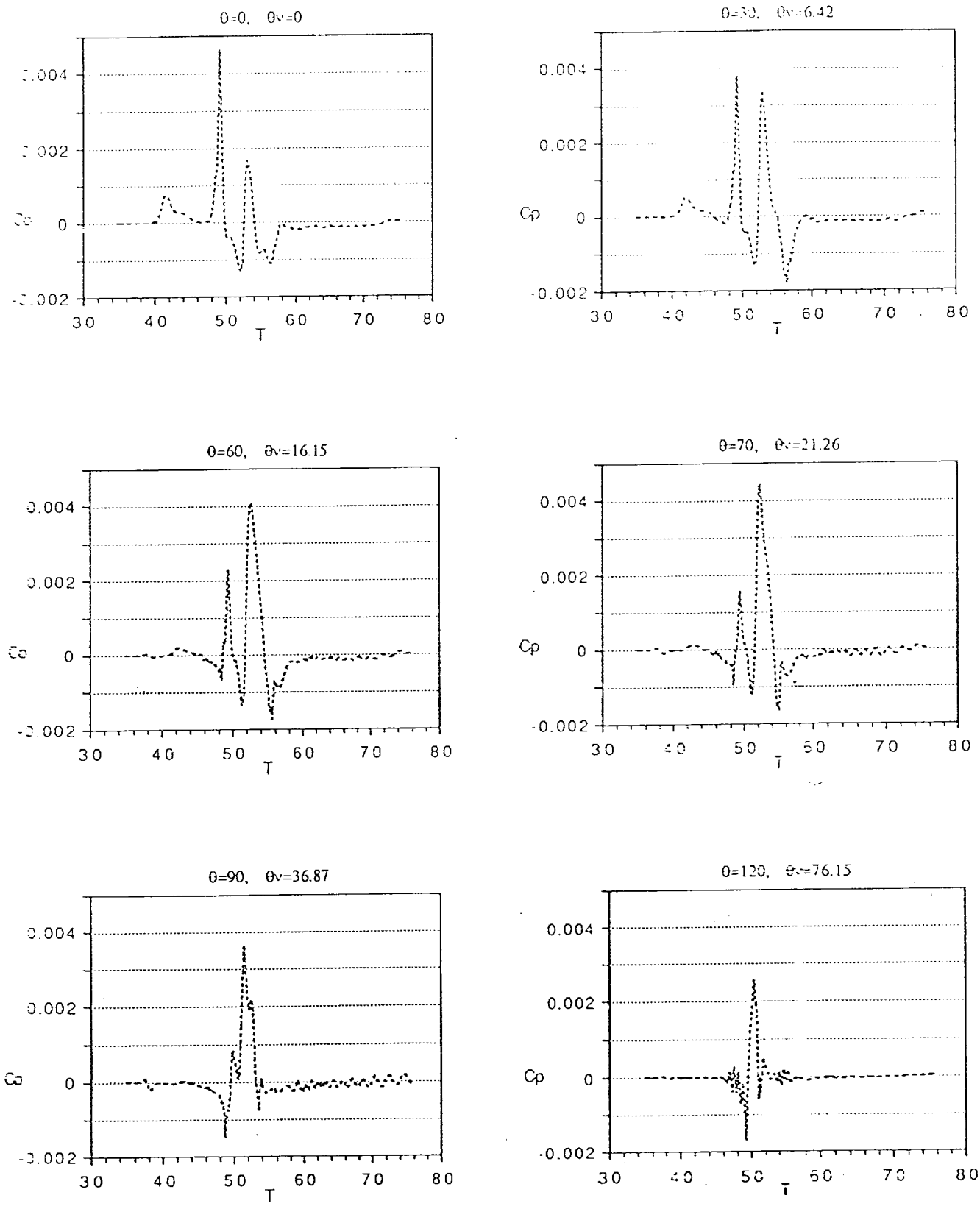

Figure 43. BVI noise directivity for airfoil SC1095rn at M_∞=0.8; r_v=50 chords, span=4 chords

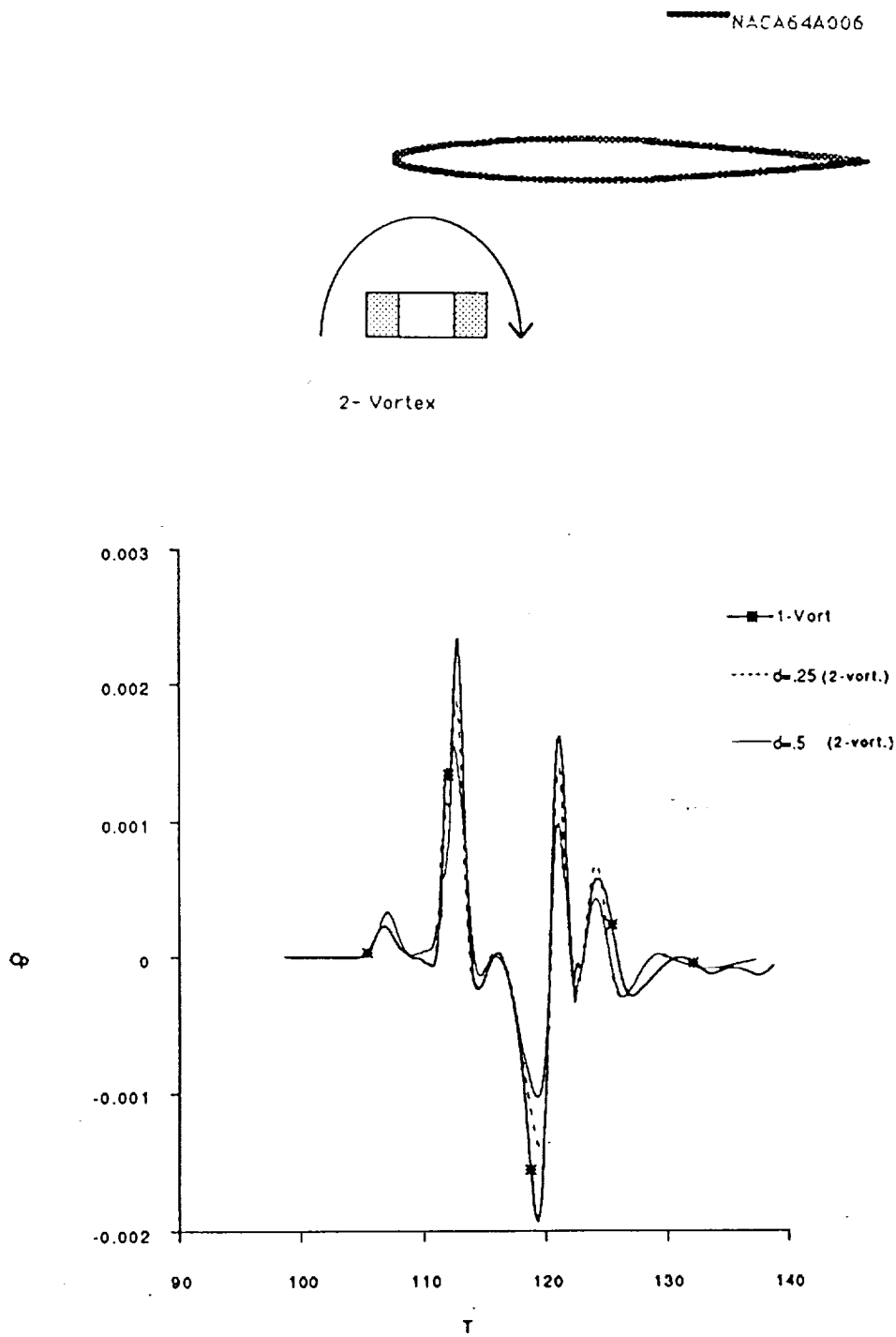

Figure 44. Vortex splitting model and far-field BVI noise (r_V=50, θ=30°).

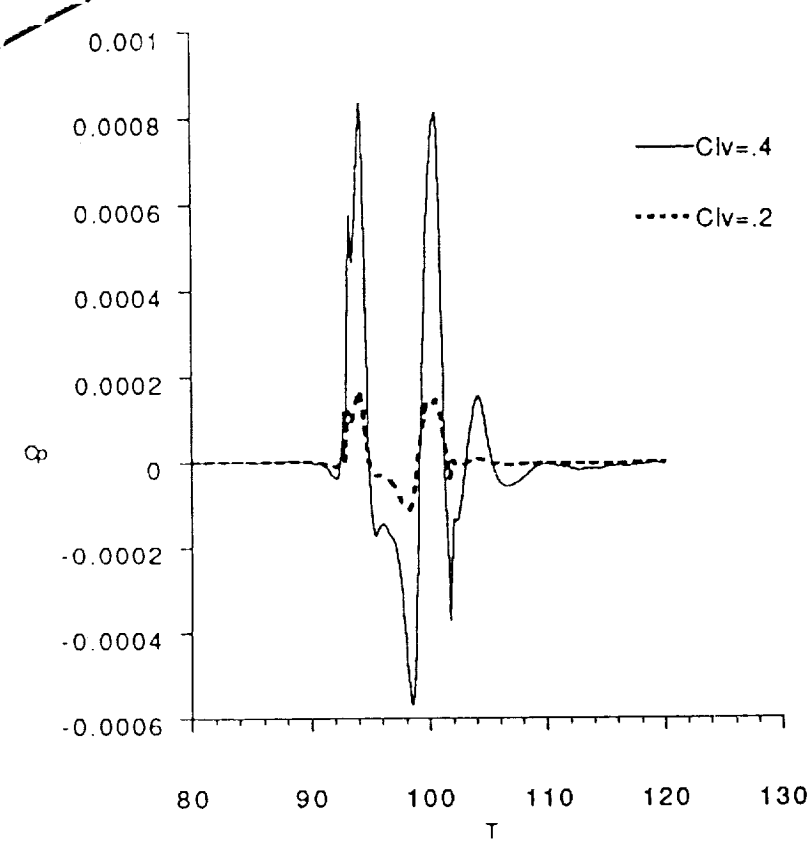

Figure 45. Effect of vortex strength on far-field BVI noise (r_V=50, θ=30°).

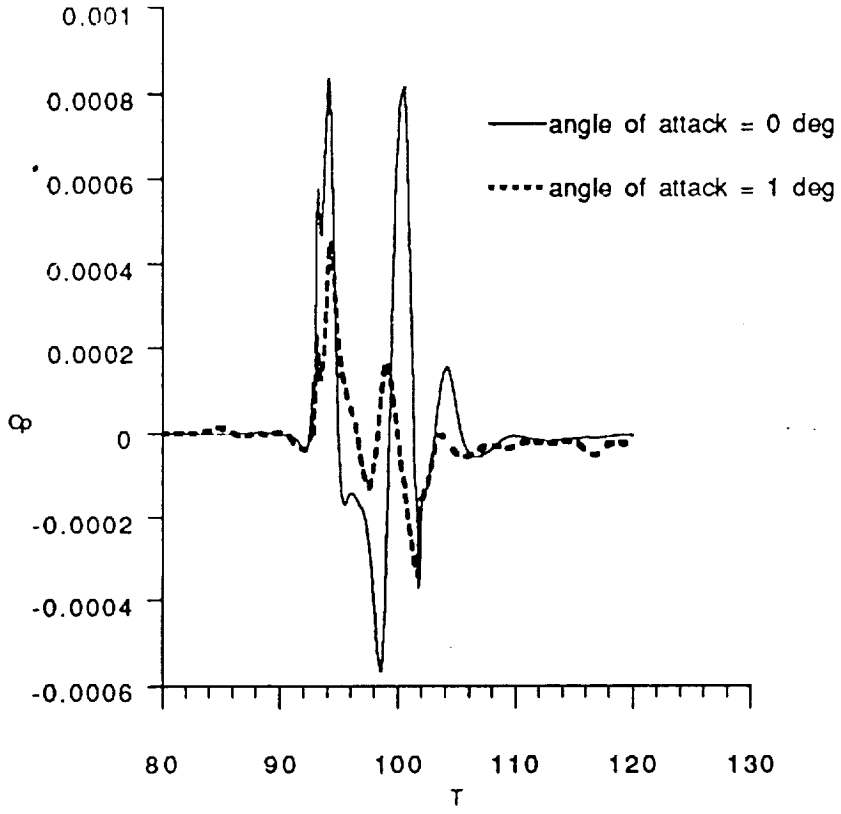

Figure 46. Effect of angle of attack on far-field BVI noise (r_V=50, θ=30°).